A NUMERICAL INVESTIGATION OF EXTENDING DIFFUSION THEORY CODES TO SOLVE THE GENERALIZED DIFFUSION EQUATION IN THE EDGE PEDESTAL

A Thesis Presented to the Academic Faculty

by

John-Patrick Floyd II

In Partial Fulfillment of the Requirements for the Degree of Master of Science

in the School of Nuclear and Radiological Engineering

Georgia Institute of Technology
May 2011

A NUMERICAL INVESTIGATION OF EXTENDING DIFFUSION THEORY CODES TO SOLVE THE GENERALIZED DIFFUSION EQUATION IN THE EDGE PEDESTAL

Approved by:

Dr. W. M. Stacey, Advisor
School of Mechanical Engineering
Georgia Institute of Technology

Dr. Nolan E. Hertel
School of Mechanical Engineering
Georgia Institute of Technology

Dr. Bojan Petrovic
School of Mechanical Engineering
Georgia Institute of Technology

Date Approved: 3/31/2011

To all of the scientist and engineers who have devoted their careers to discovering and perfecting technologies that improve the human condition.

ACKNOWLEDGEMENTS

The author would like to thank Dr. R. J. Groebner for providing the fits to the DIII-D experimental data used in this analysis and express his appreciation to the DIII-D team for the use of the data. This work was supported by the U. S. Department of Energy Grant No. DE-FG02-00-ER54538 with the Georgia Tech Research Corporation.

I would like to thank Dr. Stacey for being an excellent advisor in every way. I thank my committee members for their time and contributions. I wish to thank my parents and brother for their unfailing support of my efforts to achieve the goals I have set for myself and for the exemplary example they set for me through their actions. My eternal thanks go to my Saviour and Lord, Jesus Christ, whose strength, patience, and mercy have allowed me to complete this work. Romans 8:31.

TABLE OF CONTENTS

LIST OF TABLES

LIST OF FIGURES

SUMMARY

The presence of a large pinch velocity in the edge pedestal of high confinement (H-mode) tokamak plasmas implies that particle transport in the plasma edge must be treated by a pinch-diffusion theory, rather than a pure diffusion theory. Momentum balance also requires the inclusion of a pinch term in descriptions of edge particle transport. A numerical investigation of solving generalized pinch-diffusion theory using methods extended from the numerical solution methodology of pure diffusion theory has been carried out. The generalized diffusion equation has been numerically integrated using the central finite-difference approximation for the diffusion term and three finite difference approximations of the pinch term, and then solved using Gauss reduction. The pinch-diffusion relation for the radial particle flux was solved directly and used as a benchmark for the finite-difference algorithm solutions to the generalized diffusion equation. Both equations are solved using several mesh spacings, and it is found that a finer mesh spacing will be required in the edge pedestal, where the inward pinch velocity is large in H-mode plasmas, than is necessary for similar accuracy further inward where the pinch velocity diminishes. An expression for the numerical error of various finite-differencing algorithms is presented.

CHAPTER 1

MAGNETIC CONFINEMENT FUSION BASICS

When two atoms have sufficient kinetic energy to overcome the Coulomb barrier and fuse during a collision instead of scattering, the reaction is known as fusion. This process powers the stars, and the replication of this reaction for power production purposes has been the focus of a major research initiative since the mid-twentieth century.

1.1

Fusion in the Stars

In astral energy production, gravity confines and compresses hydrogen to form a sphere with a core at high pressure and central temperatures of around 15,700,000 K[1]. The kinetic energy of plasma particles (mostly hydrogen atoms) in the core is sufficient to ensure that some of the hydrogen atoms that physically interact with other atoms undergo fusion instead of scattering. An analogy would be a billiards player striking the cue ball with sufficient force to cause it to fuse with the target ball. Fusion of hydrogen atoms begins the proton-proton fusion chain[2] that both releases energy to maintain core temperatures and produces fuel for further fusion reactions.

1.2

Fusion on Earth

The quest to replicate the functionality of the stars and harness fusion to generate power on Earth began early in the nuclear age. In order to create the conditions necessary for fusion to occur without the benefit of gravitational compression, gaseous hydrogen must be heated into a hundred-million Kelvin plasma state and maintained at that temperature while also being effectively confined to a limited space. This confinement maximizes plasma density (to increase the fusion reaction rate) and minimizes the energy loss from the plasma due to escaping particles (to maintain high temperatures). The high plasma temperatures preclude the use of any known materials to confine the plasma, but fortunately the ionized state of the plasma particles allows direct electromagnetic manipulation. This property is utilized by employing powerful magnetic fields to compress and contain the plasma while simultaneously preventing any significant plasma-material interaction except in specially-designated areas.

Beginning in the 1950s, various magnetic confinement devices were built and found to be ineffective. However, in the 1960s, Soviet scientists designed a device they called a "tokamak" (a Russian acronym[3]) that confined the plasma in a toroidal (roughly doughnut shaped) plasma chamber using a helical magnetic field. After many years of studying methods of magnetic confinement, most scientists in the fusion field agreed that the tokamak design was a good candidate for a successful magnetic fusion reactor. The final tokamak research iteration before commercial power generation with these reactors is realized is currently under construction in Cadarache, France. The ITER device is

scheduled[4] for first plasma in 2019.

1.3

Tokamak Magnetic Confinement Fusion

When attempting to cause two elements to fuse, scientists have determined that the reaction having the lowest energy threshold for a reasonable reaction rate (and therefore requiring the lowest temperatures, which eases the demands on the magnetic fields confining a hundred million degree plasma) is a fusion reaction between the tritium and deuterium isotopes of hydrogen (^{3}H and ^{2}H). Figure 1.1 shows the reactivities of different reactions as a function of particle energy (temperature). Because tritium (^{3}H) is difficult to produce and too expensive to regularly utilize in research reactors, scientists generally use a reactor plasma composed of deuterium (^{2}H) ions, and extrapolate the results to what would be expected using a 50/50 deuterium-tritium mix.

In tokamak devices, two main magnetic fields are employed to effect the helical magnetic field that provides most of the plasma confinement. These two fields are shown in Figure 1.2 and called the poloidal and toroidal magnetic fields. Figure 1.2 also shows several important plasma regions and tokamak features and geometries. The plasma particles generally follow the helical field lines and orbit them at a distance on the order of 10^{-4} meters. The toroidal, radial, and poloidal directions comprise the toroidal coordinate system.

In a tokamak, the separatrix is the effective boundary of the plasma, and it is located just inside the first wall. The minor radius is a horizontal radius of the cross-

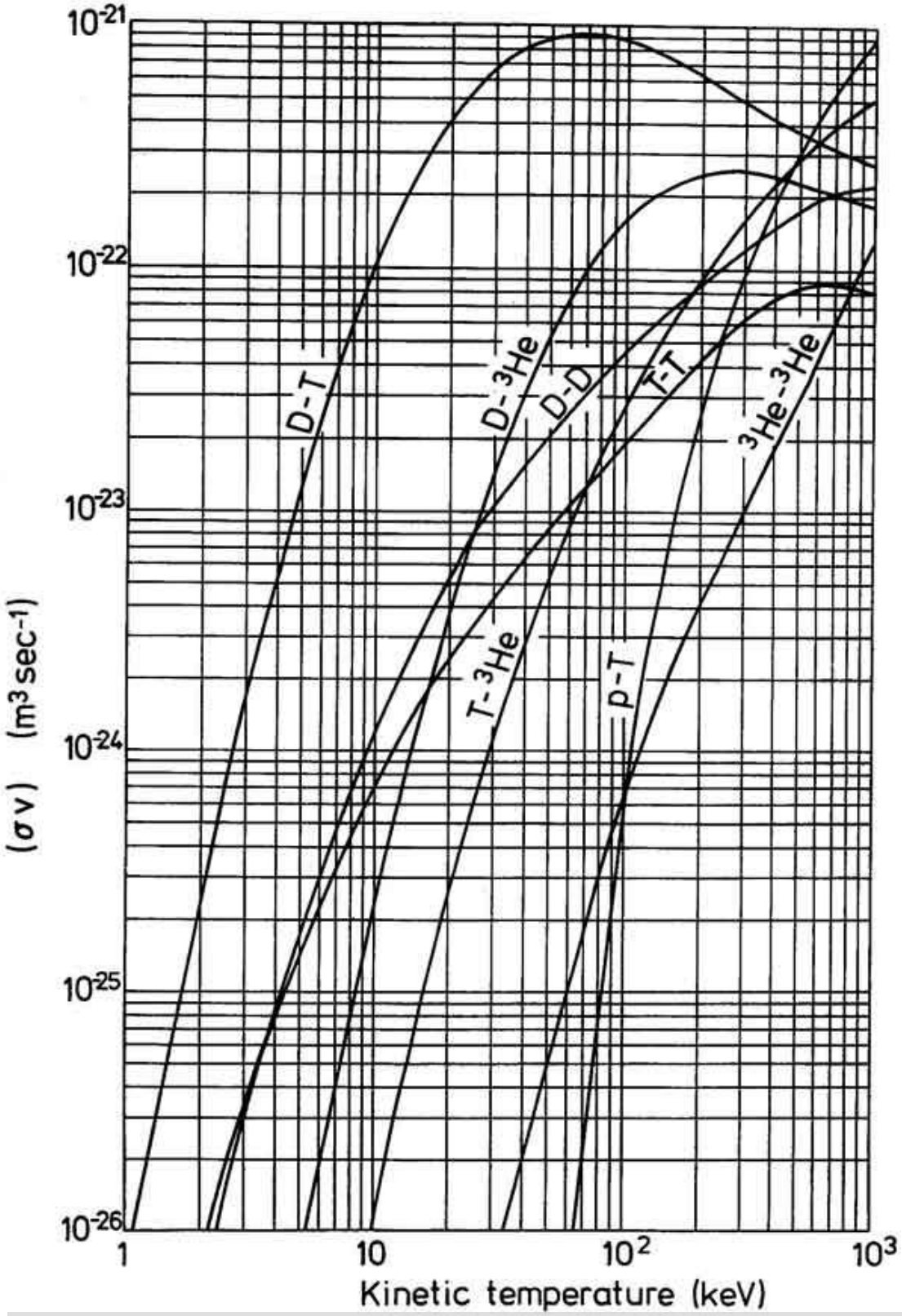

Figure 1.1 : Energy-Dependent Reactivities for Several Fusion Reactions (Ref. 5)

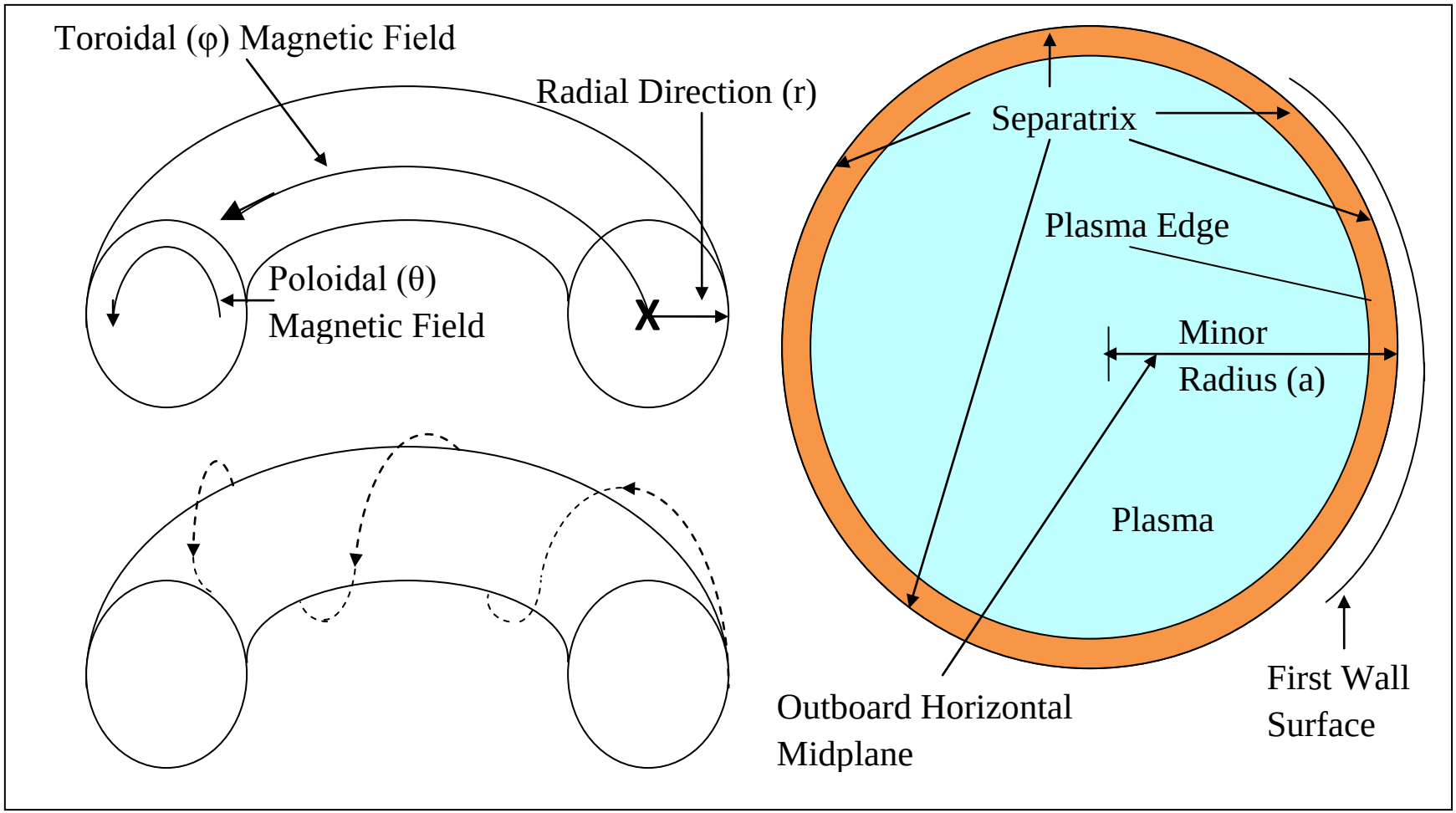

Figure 1.2 : Magnetic Fields, Directions, Regions, and Geometries of a Tokamak Plasma.

section of the plasma. The plasma does not actually have a circular cross-section, but a much more complex geometry. Scientists use the circular plasma cross-section approximation to more easily model plasmas for study. The conversion of the plasma geometry to an effective circular model will be discussed in Chapter 4.

The plasma edge is the region of the plasma near the separatrix, and it contains the edge pedestal, a region of sharp density and temperature gradients whose presence characterizes an H-mode (high confinement) plasma. The edge pedestal begins at about 94% of the normalized radius and extends to the separatrix. This "pedestal" behaviour by the temperature and density profiles of the plasma particles is shown in Figure 1.3.

Particle transport and plasma behaviour in the edge pedestal region are very important factors in tokamak performance, but they are not well understood. This work concerns plasma transport in the edge pedestal region, and is conducted using data collected from the edge region just above the outboard horizontal midplane (the minor radius that is horizontal and situated from the plasma center to the separatrix on the outer side of the plasma chamber). The data is from the General Atomics DIII-D research tokamak located in San Diego, California.

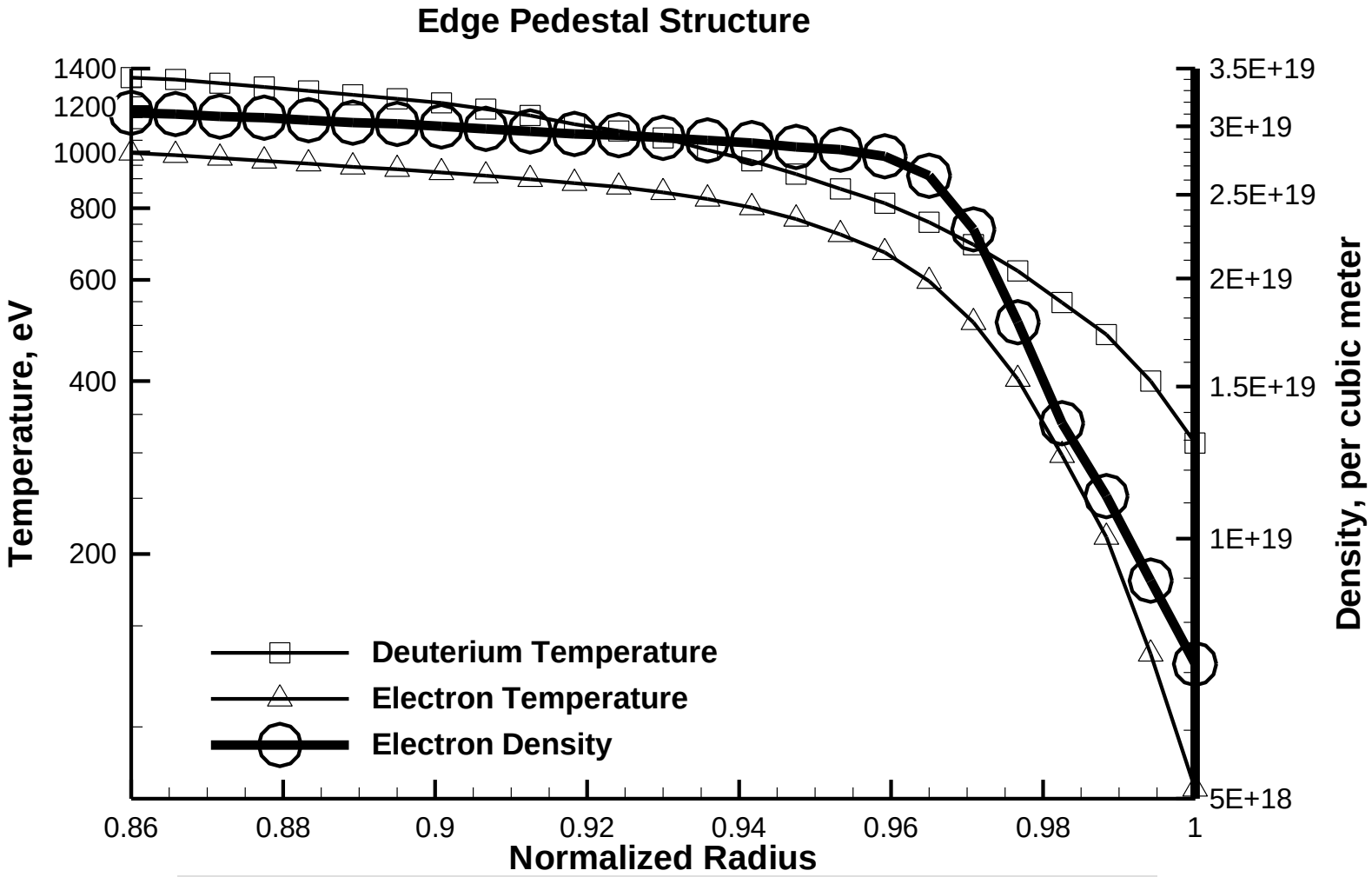

Figure 1.3 : Fitted Temperature and Electron Density Data Between ELMs.

Chapter 2

Introduction

The H-mode edge pedestal, a steep-gradient region just inside the separatrix over which the plasma pressure increases rapidly, is an area of intense research interest[6] because of experimental[7,8,9] and theoretical[10,11] evidence indicating that the performance of future tokamaks may be strongly linked to the values of the temperatures and densities at the top of the pedestal. An important extension of these studies is the development of a predictive capability for more accurate modeling of ion transport in the edge. Currently, these computational efforts center around 1.5-D and 2-D codes (e.g. ONETWO[12], GTEDGE[13], ASTRA[14], SOLPS[15], UEDGE[16,17]) which solve the plasma fluid balance equations for particle, momentum, and energy balance in one or two geometric dimensions, utilizing 1-D or 2-D calculations of recycling neutrals density.

The plasma particle transport analysis in these types of codes is usually based on a purely diffusive model of particle transport, $\Gamma = -D\nabla n$, where Γ is the particle flux, n is the particle density, and D represents the diffusion coefficient. In these codes, the diffusion coefficients are adjusted to provide a match of measured density profiles in a few locations. The use of this "diffusion theory methodology" to interpret diffusion coefficients from experimental density profiles often produces unrealistically small values[18]. This result prompted an investigation into the form of the particle transport flux required by particle and momentum balance[19], which determined that the ion radial transport flux must satisfy a pinch-diffusion relationship, $\Gamma = -D\nabla n + nV_r^{pinch}$, where V_r^{pinch} is the pinch velocity, and not a purely diffusive relationship, $\Gamma = -D\nabla n$.

Substitution of this pinch-diffusion relation into the continuity equation leads to a generalized diffusion equation including diffusive second-derivative terms and convective first-derivative terms incorporating the pinch velocity[20]. This raises the question of modifying the existing codes mentioned above, most of which are based on a pure diffusion relation for the radial particle flux, to solve the generalized diffusion equations, which contain an additive first derivative term involving the pinch velocity.

The purpose of this thesis is to report on a first numerical investigation into the adaptation and extension of a purely diffusive numerical solution method to the pinch-diffusion formalism.

Chapter 3

Force Balance, Particle Transport, the Pinch-Diffusion Model, and the Generalized Diffusion Equation

The idea that the centrally-peaked density profiles observed in edge-fueled tokamaks are evidence of an inward particle pinch is as old as tokamak research itself[21,22], and many researchers represent the total radial particle flux as a diffusive component plus a convective component (e.g. Ref. 23).

$$\Gamma = -D\nabla n + nV_r^{pinch} \tag{1}$$

Detailed numerical modeling exercises[24] of DIII-D[25] discharges were found to require the use of such a pinch term in order to obtain reasonable agreement with experiment. More recent interpretive calculations[26] of DIII-D have inferred an inward particle flux early in the H-mode phase, which would require a particle pinch. The experimental observations of pedestal density[27] and electron density barrier width expansions in time between ELMs[28] in DIII-D can be attributed to an inward pinch. Two-dimensional modeling of JET discharges in a configuration optimized for edge diagnostics also demonstrated that either a pinch velocity or a spatially-varying diffusion coefficient is required to explain the observed density profiles and calculated particle source profiles[29]. These findings motivate the present work.

3.1

Force Balance and Particle Transport

The time-independent momentum balance equation for ion species "j" is

$$\nabla\bullet\left(n_j m_j \vec{V}_j \vec{V}_j\right)+\nabla p_j+\nabla\bullet\vec{\pi}_j = n_j e_j\left(\vec{V}_j\times\vec{B}\right)+n_j e_j\vec{E}+\vec{F}_j+\vec{M}_j-n_j m_j \nu^j_{elcxj}\vec{V}_j \tag{2}$$

where n_j is the ion density, m_j is the ion mass, the vector V_j is the ion velocity vector, p_j is the ion pressure, the tensor π_j respresents the ion viscous momentum flux, e_j is the ion charge, the vector B is the magnetic field, the vector E represents the electric field, the vector F_j represents the interspecies collisional friction, the vector M_j represents the external momentum input rate to the ions, and ν^j_{elcxj} is the ion momentum loss rate due to elastic scattering and charge exchange with neutrals of all ion species 'k' (impurities). The flux surface average (FSA) radial component of Eq. (2) may be written to leading order as

$$E^0_r=\frac{1}{n^0_j e_j}\frac{\partial p_j}{\partial r}+V^0_{\phi j}B^0_\theta-V^0_{\theta j}B^0_\phi \tag{3}$$

where E_r is the radial electric field, $V_{\phi j}$ is the ion toroidal rotation velocity, $V_{\theta j}$ is the ion poloidal rotation velocity, B_ϕ is the toroidal magnetic field, and B_θ is the poloidal magnetic field. The FSA toroidal component can be written to leading order as[20]

$$n^0_j m_j \nu^0_{jk}\left(\left(1+\beta_j\right)V^0_{\phi j}-V^0_{\phi k}\right)=n^0_j e_j E^A_\phi+e_j B^0_\theta\Gamma_{rj}+M^0_{\phi j} \tag{4}$$

where $\beta_j\equiv\frac{\nu_{dj}}{\nu^0_{jk}}$, $V_{\phi k}$ is the impurity toroidal rotation velocity, $M_{\phi j}$ is the external toroidal momentum input rate to the ions, E^A_ϕ is the electromagnetically induced toroidal

electric field, and Γ_{rj} is the radial ion flux. The term ν_{jk} represents the interspecies collision frequency (a sum over all other species $k \neq j$ is implied). The term v_{dj} represents the experimental rate of radial transfer of toroidal angular momentum, and is further discussed in Chapter 5.

3.2

The Pinch-Diffusion Equation

Solving Eq. (3) for the ion and impurity toroidal rotation velocities

$$\begin{aligned} \frac{E_r}{B_\theta} - \frac{1}{n_j e_j B_\theta}\frac{\partial p_j}{\partial r} + \frac{V_{\theta j} B_\phi}{B_\theta} &= V_{\phi j} \\ \frac{E_r}{B_\theta} - \frac{1}{n_k e_k B_\theta}\frac{\partial p_k}{\partial r} + \frac{V_{\theta k} B_\phi}{B_\theta} &= V_{\phi k} \end{aligned} \tag{5}$$

and substituting them into Eq. (4), then splitting pressure into density and temperature via

$$p_j = n_j T_j \tag{6}$$

results in a multi-species pinch-diffusion relation for the radial ion flux

$$\Gamma_{rj} \equiv n_j D_{jj}\left(L_{nj}^{-1} + L_{Tj}^{-1}\right) - n_j D_{jk}\left(L_{nk}^{-1} + L_{Tk}^{-1}\right) + n_j V_{rj}^{pinch} \tag{7}$$

where the gradient scale lengths of ion and impurity density and temperature are defined as $L_x^{-1} \equiv -\left(\frac{1}{x}\frac{\partial x}{\partial r}\right)$. The "diffusion coefficients" D_{jj} and D_{jk} are

$$D_{jj} \equiv \frac{m_j T_j\left(\nu_{dj} + \nu_{jk}\right)}{\left(e_j B_\theta\right)^2}, \quad D_{jk} \equiv \frac{m_j T_k \nu_{jk}}{e_j e_k \left(B_\theta\right)^2} \tag{8}$$

where T_j and T_k are the ion and impurity temperatures, and e_k is the impurity charge.

The radial ion pinch velocity V_{rj}^{pinch} is

$$V_{rj}^{pinch} \equiv -\frac{M_{\phi j}}{n_j e_j B_\theta} - \frac{E_\phi^A}{B_\theta} + \frac{m_j \nu_{dj} E_r}{e_j B_\theta^2} + \frac{m_j B_\phi}{e_j B_\theta^2}\left(\left(\nu_{jk} + \nu_{dj}\right)V_{\theta j} - \nu_{jk} V_{\theta k}\right) \tag{9}$$

To avoid introducing uncertainty into these calculations by relying on approximate models of impurity density and charge state, several assumptions[20] have been made about the impurity ions in the edge. These assumptions are: 1. that ^{12}C is the only impurity species present, 2. it is fully ionized (+6 charge), 3. it has the same edge density profile shape as the main ions, 4. it has the same local temperature as the main ions, and 5. the ^{12}C (6+) density is 4% of the main ion density.

Using these assumptions about the carbon impurity (k) distribution, Eq. (7) can be rewritten to obtain[30] a pressure pinch-diffusion relation for the main ion (j) radial particle flux

$$\Gamma_j \equiv n_j V_{rj} = -\frac{n_j D_j}{p_j}\frac{\partial p_j}{\partial r} + n_j V_{rj}^{pinch} \tag{10}$$

Throughout the remainder of this text, when a reference to the pinch-diffusion relation is made, it refers to Eq. (10). Equation (10) provides insight into the physical effects and the various forces involved in plasma ion transport.

These carbon assumptions allow the diffusion coefficients of Eq. (8) can be reduced to

$$D_j = \frac{m_j T_j \nu_{jk}}{\left(e_j B_\theta\right)^2}\left[1 + \frac{\nu_{dj}^*}{\nu_{jk}} - \frac{Z_j}{Z_k}\right] \tag{11}$$

instead of two coefficients with slightly different coefficients proportional to the carbon density and temperature gradients. In Eq. (11), Z_j and Z_k represent the atomic number of the "j" and "k" species, in this case deuterium and carbon.

The pinch velocity from Eq. (9) becomes

$$V_{rj}^{pinch} = \frac{-M_{\phi j}}{n_j e_j B_\theta} - \frac{E_\phi^A}{B_\theta} + \frac{m_j \left(\nu_{jk} + \nu_{dj}^*\right)\left(B_\phi V_{\theta j} + E_r\right)}{e_j B_\theta^2} - \frac{m_j \nu_{jk} V_{\phi k}}{e_j B_\theta} \tag{12}$$

These simplifying assumptions will also preclude the need for a second generalized diffusion equation for the carbon density[20].

3.3

The Generalized Diffusion Equation

The pinch-diffusion relation for the radial particle flux [Eq. (10)], can be substituted into the time-independent particle continuity equation for ion species j

$$\nabla \bullet \Gamma_j \equiv \nabla \bullet n_j \vec{V}_j = S_j \tag{13}$$

resulting in

$$\nabla \bullet \Gamma_j = \nabla \bullet \left(-\frac{n_j D_j}{p_j} \frac{\partial p_j}{\partial r} + n_j V_{rj}^{pinch} \right) = S_j \tag{14}$$

where S_j is the ionization source rate.

By using Eq. (6), it is possible to obtain from Eq. (14) a generalized diffusion equation for the pressure[20]

$$-\frac{\partial}{\partial r}\left(\frac{D_j}{T_j} \frac{\partial p_j}{\partial r} \right) + \frac{\partial}{\partial r}\left(\frac{p_j V_{rj}^{pinch}}{T_j} \right) = S_j \tag{15}$$

Chapter 4

Measured and Calculated Data from DIII-D H-Mode Shot 98889

The DIII-D shot used in this research is discharge 98889, which has been well characterized. Selected parameters of shot 98889 are shown in Table 4.1.

Table 4.1: The Parameters of Shot 98889, an H-Mode Discharge on DIII-D.

Time Range	3.75-4.11s	Divertor Configuration	Lower Single Null
Plasma Current I_p	1.2 MA	Poloidal Field	0.22 T
Toroidal Field	2.01 T	Toroidal Electric Field	.04 V/m
Major Radius R	1.75 m	Triangularity δ	.135
Minor Radius	0.60 m	Elongation κ	1.75

The non-circular geometry of the plasma flux surfaces was modeled by an effective circular model, which is an approximate flux-surface average model that conserves flux surface area and is shown in Figure 4.1.

The experimental data used in this paper were taken just above the outboard horizontal midplane (shown in Figure 1.2). The Miller equilibrium model[31] was used to map the measured data to the flux surfaces, and the data was averaged over each flux surface to obtain flux surface averaged values. These values were then plotted as a function of the normalized radius for analysis. The radius of the effective circular model is $\bar{r} = r\sqrt{0.5\left(1+\kappa^2\right)}$ which leads to an effective minor radius of $\bar{a}$ = .86 m. The normalized radius is $\rho = \bar{r} / \bar{a}$. The measurement and data preparation techniques used

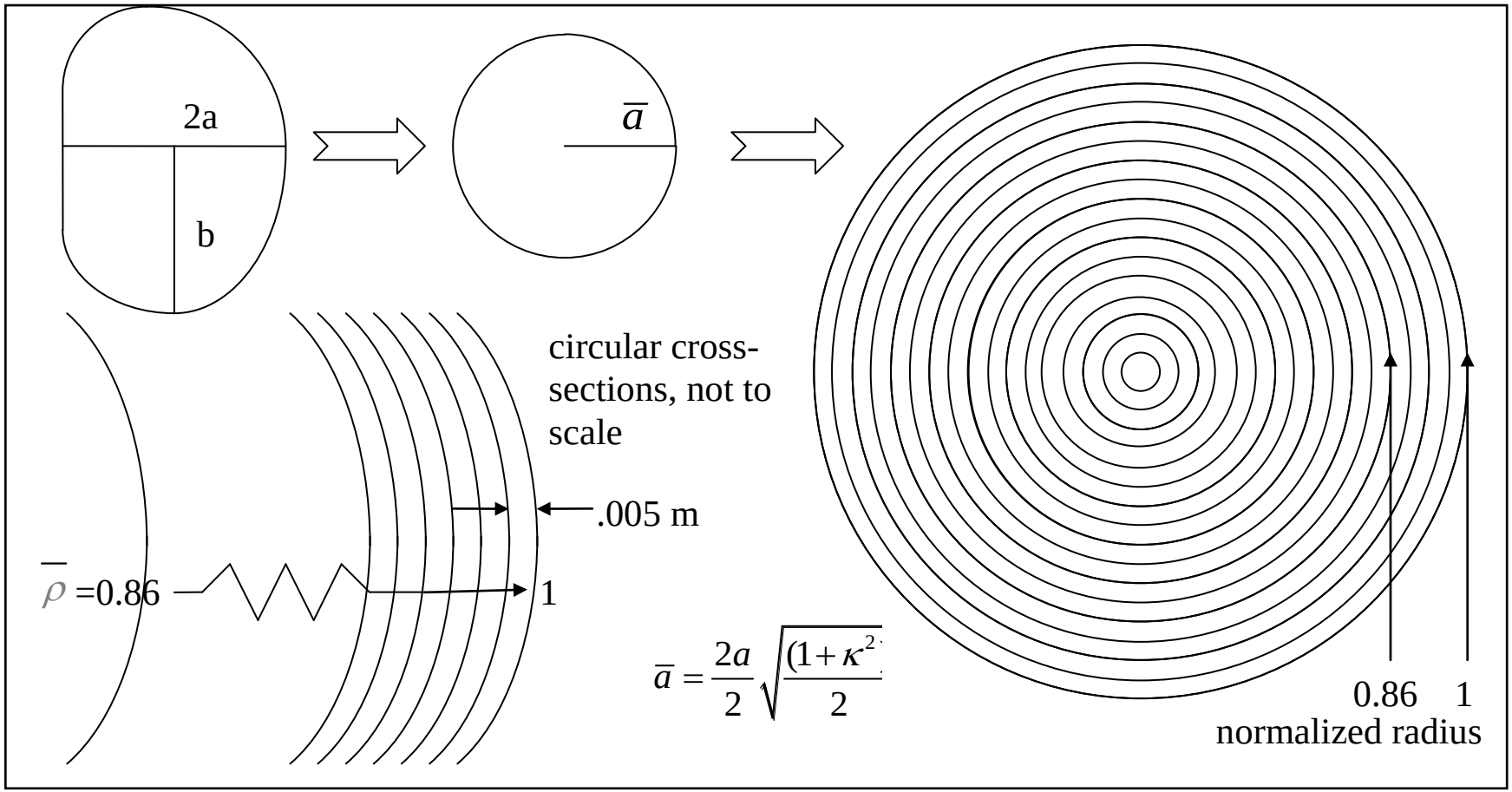

Figure 4.1 : An Illustration of the Geometric Manipulation to Obtain Data Points for the DIII-D Shot 98889.

to obtain and process the data are further described in Ref. 18.

Values for the parameters with radial dependence were taken at 25 points between the separatrix at $\rho = 1.0$ ($\bar{r} = \bar{a} = .86\,m$) and the inside of the H-mode edge pedestal at $\rho = .86$ ($\bar{r} = .74\,m$) at intervals of $\bar{r} = .005\,m$ [32]. Calculations using a finer mesh spacing were enabled by assuming a linear interpoint parameter profile.

4.1

Minimization of Error from Edge Localized Mode (ELM) Activity

ELMs in H-mode tokamak discharges are phenomena that periodically cause partial collapses of the temperature and density gradients that characterize the edge pedestal. These gradients are then rebuilt before the occurrence of the next ELM disruption. In order to minimize random error associated with inadvertent data collection during ELMs, data was collected during the intervals between sequential ELMs, and averaged over several of these intervals[32].

4.2

Measured and Explicitly Calculated Variables: $m_j, e_j, \nu_{jk}, E_\phi^A, B_\theta, B_\phi, M_{\phi j}$

The mass of a deuterium atom m_j is 3.343×10^{-27} kg. The charge e_j is 1.6022×10^{-19} C. The collision frequency between ions and impurities in the plasma ν_{jk} can be calculated from the experimentally known density and temperature profiles[30] and is shown in Figure 4.2. The electromagnetically induced toroidal electric field E_ϕ^A is a

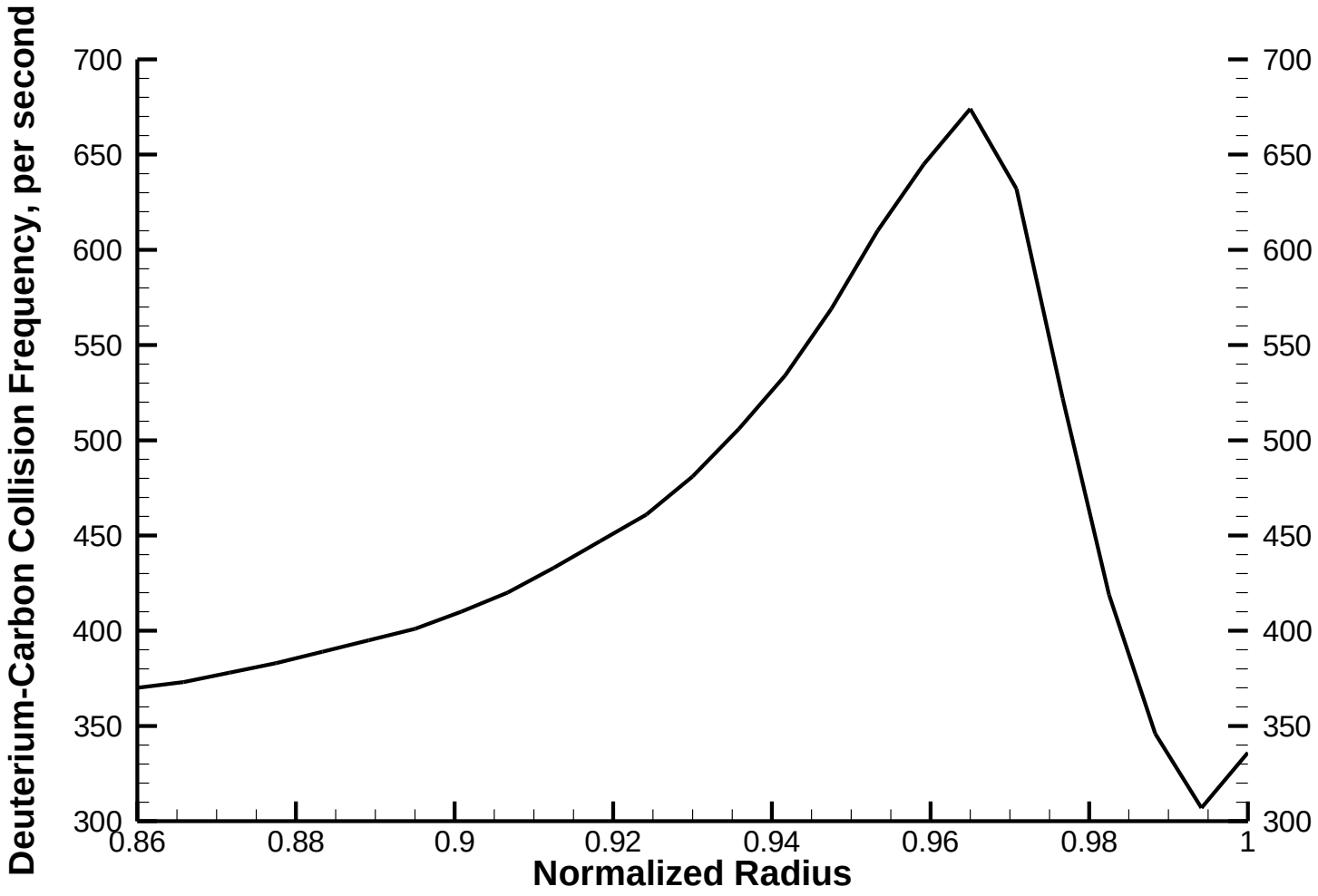

Figure 4.2 : The Deuterium-Carbon Collision Frequency.

small term with a value of 0.04 V/m, and is determined from the measured loop voltage. The poloidal magnetic field B_θ is 0.2242 T and the toroidal magnetic field B_φ is -2.01 T; these are both readily measured. The external toroidal momentum input rate from the neutral beam heating system $M_{\varphi j}$ is another small term near the separatrix, and it can be calculated from the known beam geometry and power input. This profile is shown in Figure 4.3.

4.3

The DIII-D Charge Exchange Recombination (CER) Spectroscopy system :

$$T_j, E_r, V_{\theta k}, V_{\phi k}$$

The CER system installed on DIII-D allows for the temporal and spatial resolution of the ion temperature T_j, the radial electric field E_r, and the impurity poloidal and toroidal rotation velocities $V_{\theta k}$ and $V\varphi_k$ through detection of the spectral lines from charge exchange recombination between neutral atoms and fully-stripped ions[33].

The ion temperature profile, show in Figure 1.3, is characteristic of an H-mode discharge. The radial electric field, shown in Figure 4.4, sharply drops toward the separatrix to values of less than -1.0×10^5 V/m, and is active in the edge at large magnitudes, making it a major contributor to the pinch velocity.

Carbon toroidal and poloidal rotation velocities, which are used in calculating the poloidal and toroidal rotation speeds of the deuterium ions, were obtained using the CER spectroscopy system. Figure 4.5 shows a fit to the measured toroidal and poloidal rotation velocities for the $^{12}C^{6+}$ impurity.

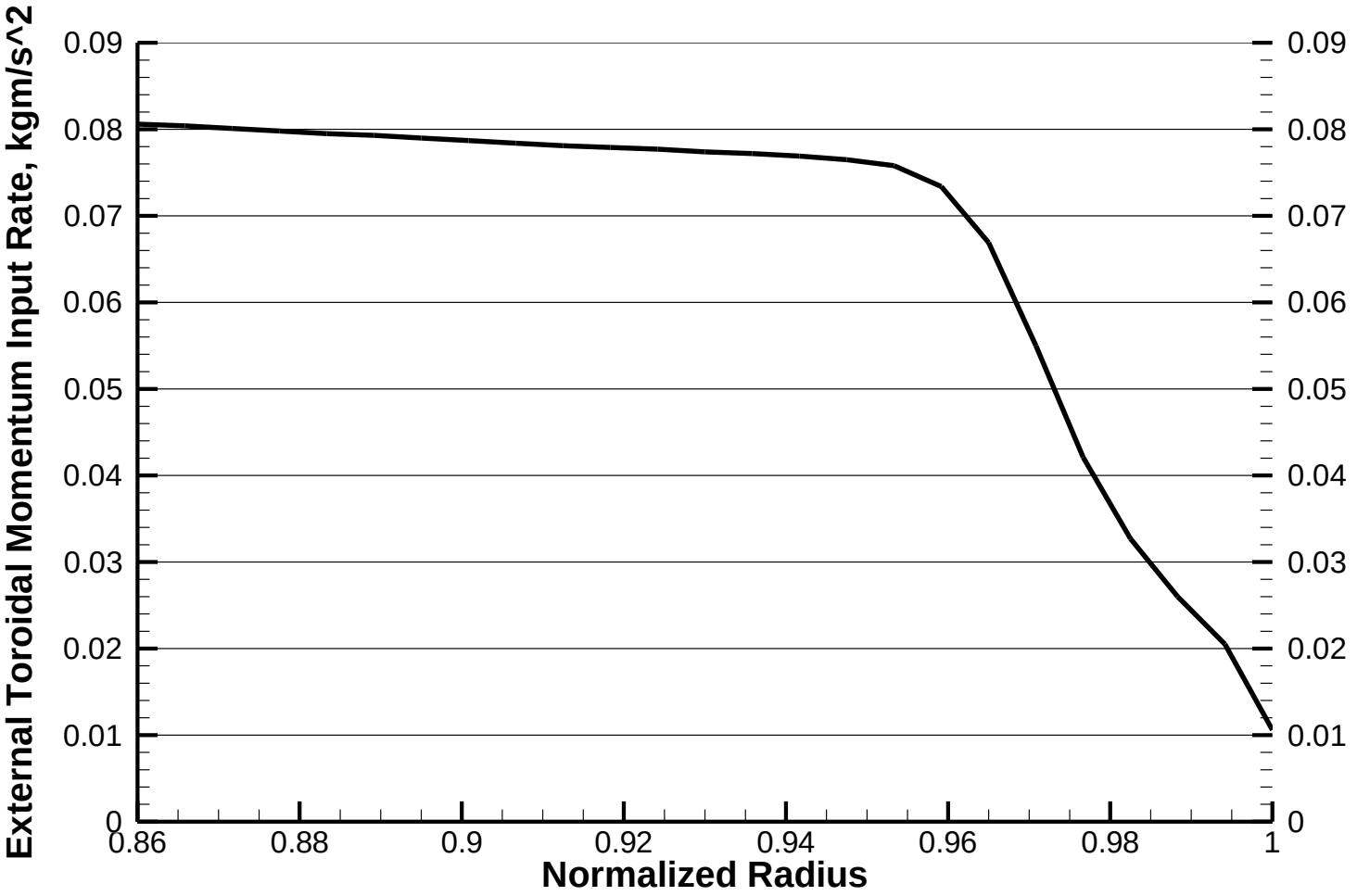

Figure 4.3 : The External Toroidal Momentum Input Rate.

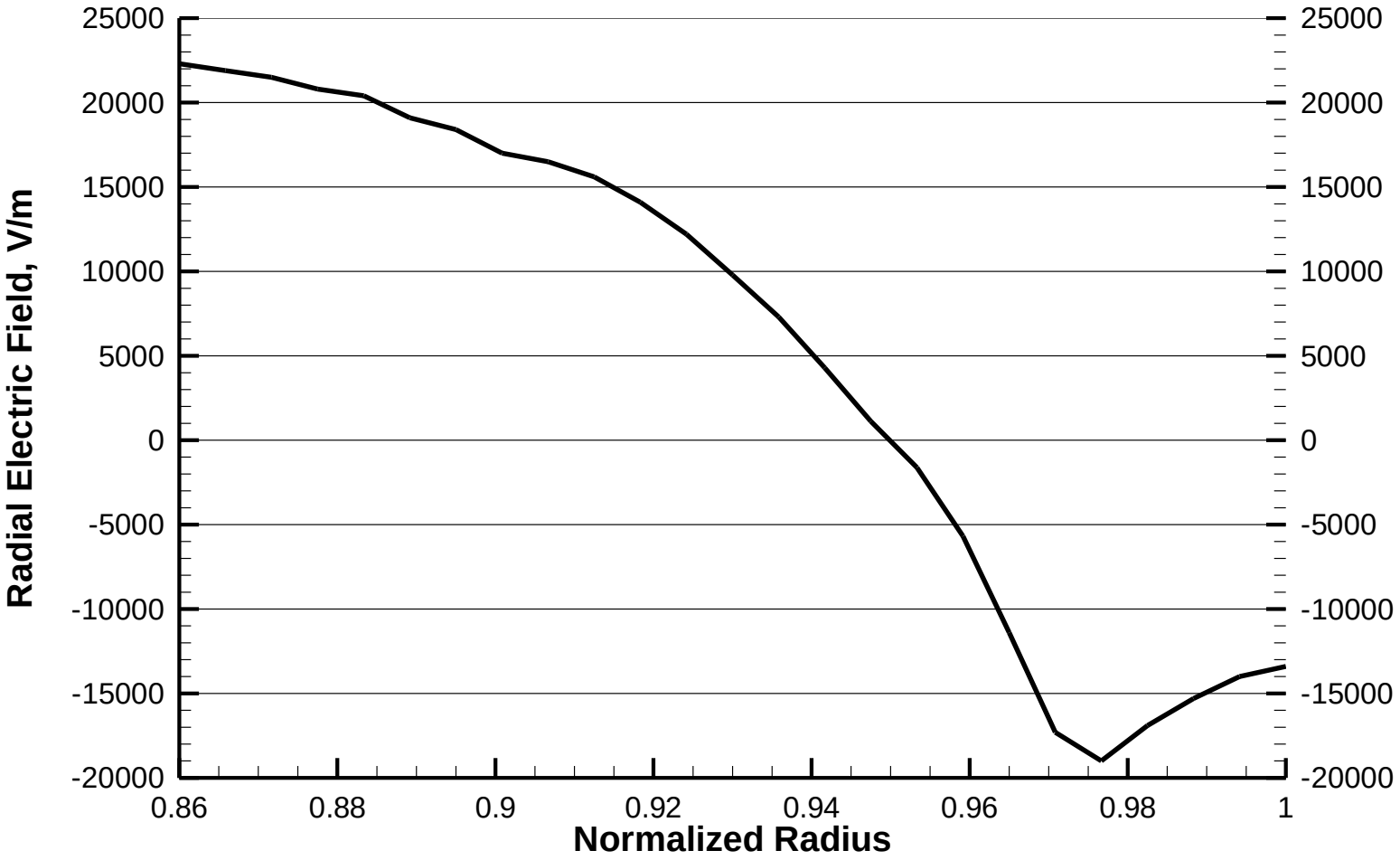

Figure 4.4 : The Radial Electric Field

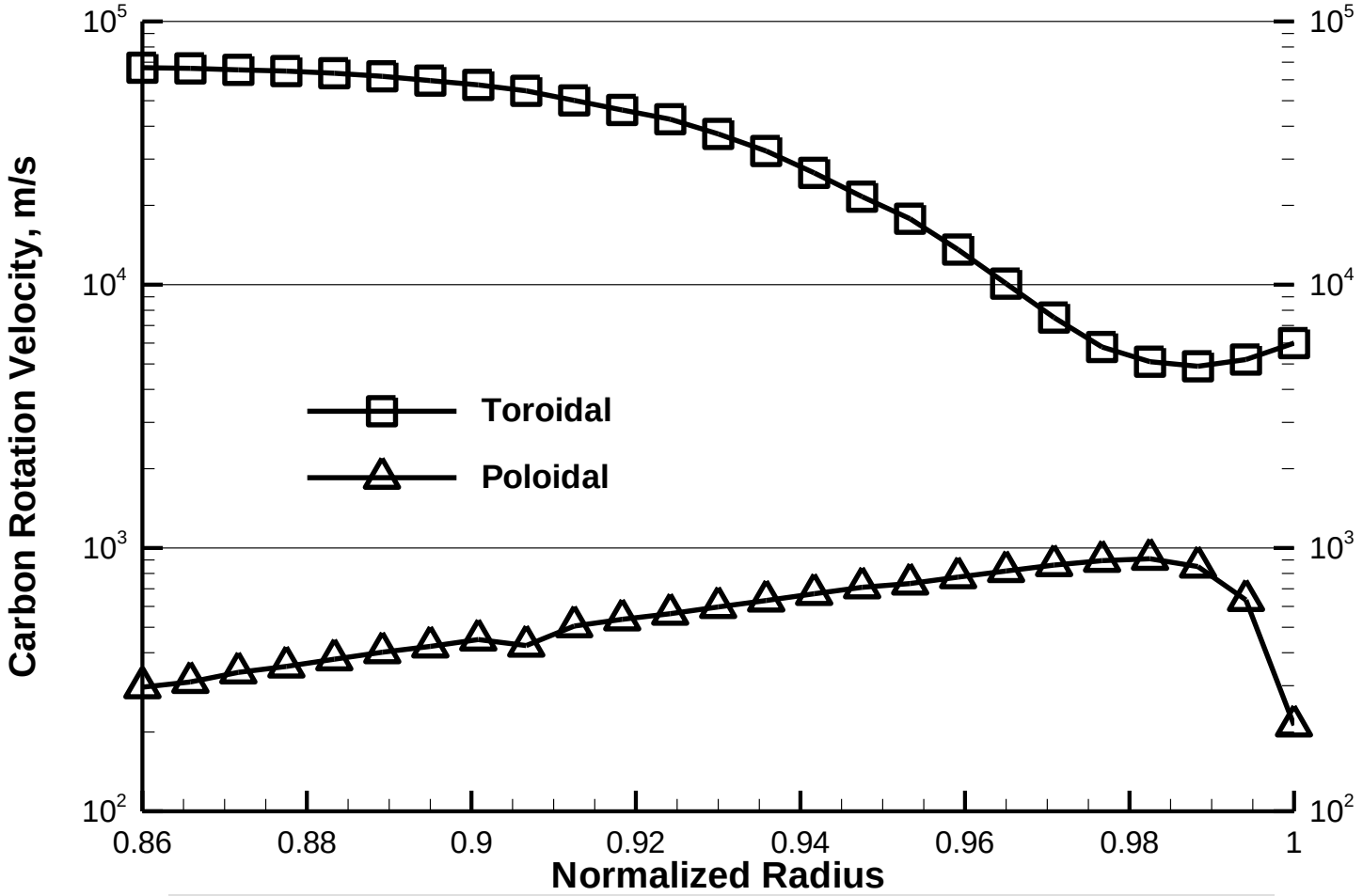

Figure 4.5 : Carbon Toroidal and Poloidal Rotation Velocities

4.4

The Thomson Scattering Diagnostics System: n_e, T_e, n_j

The electron temperature T_e and electron density n_e profiles were experimentally measured by the 40 spatial channel Thomson scattering diagnostics system installed in DIII-D[34]. The electron temperature and density are both shown in Figure 1.3. The ion density n_j is a slightly smaller, nearly scaled version of the electron density which is calculated using the electron density and the carbon density assumptions. All three profiles exhibit classic H-mode behaviour in the edge pedestal.

4.5

Deuterium Ionization Source Rate: S_j

The deuterium ionization source rate S_j is the rate at which neutral deuterium atoms are ionized. These neutral atoms are mostly plasma ions that have escaped confinement, collided with the first wall, gained electrons to become neutral, and returned to the plasma to be re-ionized. Equation (13) defines the relationship between the radial ion flux (Γ_{rj}) and the deuterium ionization source rate. This source rate is defined as $S_j = n_e n_0 \langle \sigma v \rangle_{ion}$, where n_0 is the recycling neutrals density, and the last term is the reactivity. S_j was calculated with the GTEDGE integrated modeling code[13] using a 2D neutral transport calculation coupled to a two-point divertor model and a core global particle and power balance. The deuterium ionization source rate is shown in Figure 4.6.

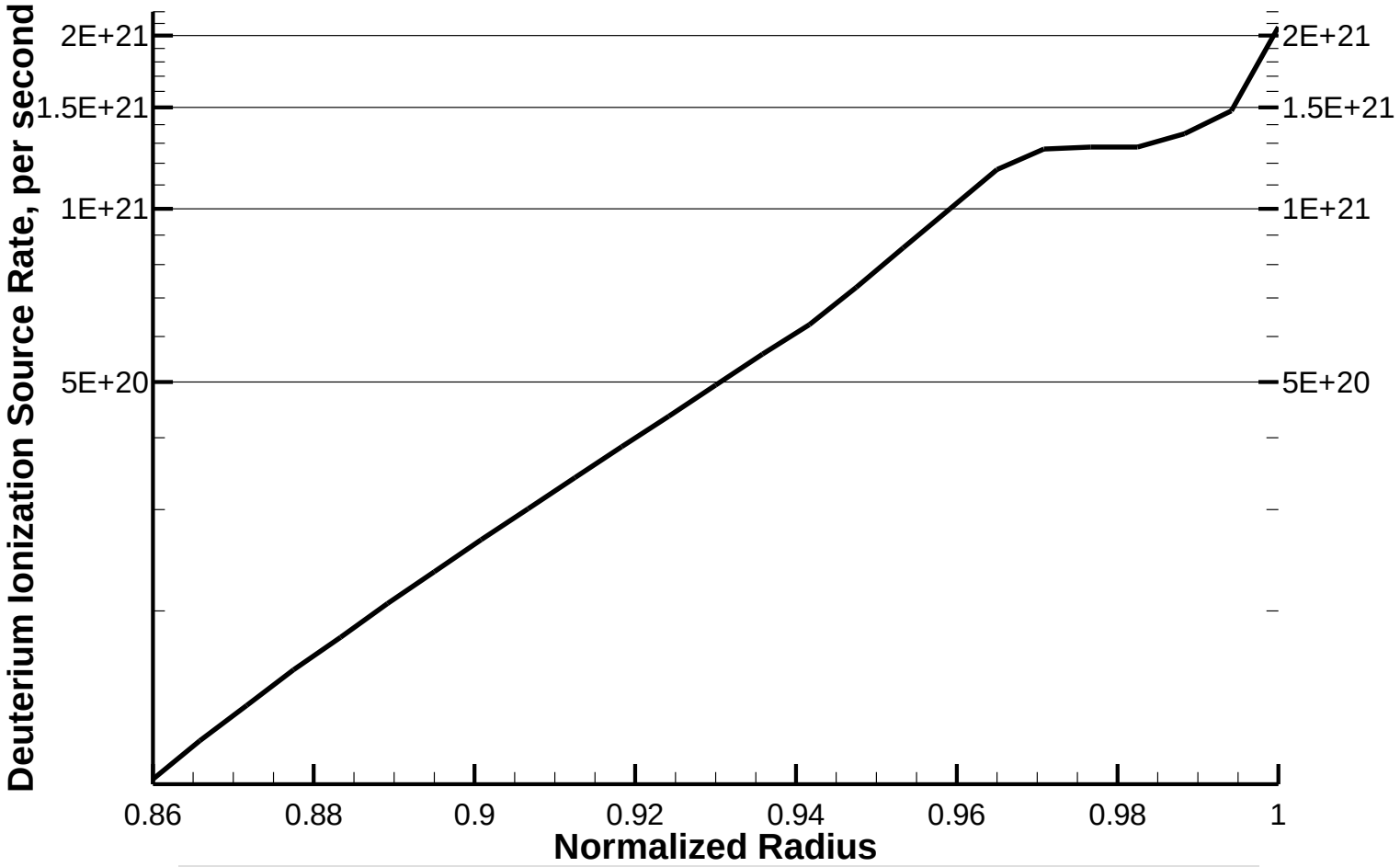

Figure 4.6 : The Deuterium Ionization Source Rate.

Chapter 5

Derived and Calculated Parameters, and the Pinch Velocity and Diffusion Coefficient

5.1

Experimental Rate of Radial Transfer of Toroidal Angular Momentum : ν_{dj}

The term ν_{dj} represents an aggregation of the momentum transfer frequencies of various phenomena

$$\nu_{dj} \equiv \nu_{gvj} + \nu_{\perp j} + \nu_{anomj} + \nu_{nj} + \nu_{elcxj} + \nu_{ionj} \tag{16}$$

including the gyroviscous ν_{gvj} and perpendicular $\nu_{\perp j}$ components of the neoclassical viscous torque, the turbulent (anomalous) toroidal viscous torque ν_{anomj}, the two components of the inertial term, ν_{nj} and an ionization term ν_{ionj}, and the ion momentum loss rate associated with elastic scattering and charge exchange ν_{elcxj} between the ions and neutral impurities[20].

To obtain a profile for this term ν_{dj}, measured rotation velocities are used as an input to solve Eq. (4) backwards and infer the value of this momentum transfer frequency[30]. First, Eq. (4) is rearranged into an expression for ν_{dj}

$$\nu_{dj} = \nu_{jk}\left[\frac{n_j e_j E_\phi^A + e_j B_\theta \Gamma_{rj} + M_{\phi j}}{n_j m_j \nu_{jk} V_{\phi j}} - \left(1 - \frac{V_{\phi k}}{V_{\phi j}}\right)\right] \tag{17}$$

which defines a relationship that ν_{dj} must satisfy in order to produce the measured

rotation velocities. A similar expression can be obtained for the k species with the j's and k's interchanged in the two-ion model. All the values on the right side of the equation can be measured or calculated with the exception of the deuterium toroidal rotation velocity. In order to find a profile for the deuterium toroidal rotation velocity, a perturbation analysis is used to obtain an estimate of the difference between the measurable carbon toroidal rotation velocity and the problematic deuterium toroidal rotation velocity.

In the perturbation analysis, a separate Eq. (4) for each species j and k are added to eliminate the v_{jk} friction terms, and a definition for the effective v_{dj} is derived

$$\begin{aligned} v_d^{eff} &\equiv \frac{n_j n_j v_{dj} + n_k m_k v_{dk}}{n_j m_j + n_k m_k} \\ &= \frac{\left(n_j e_j E_\phi^A + e_j B_\theta \Gamma_{rj} + M_{\phi j}\right) + \left(n_k e_k E_\phi^A + e_k B_\theta \Gamma_{rk} + M_{\phi j}\right) - \left[n_j m_j v_{dj}\left(V_{\phi j} - V_{\phi k}\right)\right]}{\left(n_j m_j + n_k m_k\right) V_{\phi k}} \end{aligned} \tag{18}$$

The last term in the numerator is set to zero to obtain a zeroth order approximation of v_d^{eff}

$$v_d^0 \equiv \frac{\left(n_j e_j E_\phi^A + e_j B_\theta \Gamma_{rj} + M_{\phi j}\right) + \left(n_k e_k E_\phi^A + e_k B_\theta \Gamma_{rk} + M_{\phi j}\right)}{\left(n_j m_j + n_k m_k\right) V_{\phi k}} \tag{19}$$

Along with the measured carbon toroidal rotation velocity, Eq. (19) is used in Eq. (4) for the ion species "k" to obtain a zeroth order approximation for the difference between the carbon and deuterium toroidal rotation velocities.

$$\left(V_{\phi j} - V_{\phi k}\right)_0 = \frac{n_j e_j E_\phi^A + e_j B_\theta \Gamma_{rj} + M_{\phi j} - n_j m_j v_d^0 V_{\phi k}^{\exp}}{n_j m_j \left(\nu_{jk} + \nu_d^0\right)} \tag{20}$$

This approximation is then used in Eq. (4) for the k species to solve for v_{dk}.

$$v_{dk} = \frac{\left(n_k e_k E_\phi^A + e_k B_\theta \Gamma_{rk} + M_{\phi j}\right) + n_k m_k \nu_{kj} \left(V_{\phi j} - V_{\phi k}\right)_0}{n_k m_k V_{\phi k}^{\exp}} \tag{21}$$

The deuterium experimental rate of radial transfer of toroidal angular momentum is then calculated from Eq. (19) using $\nu_d^{eff} \approx \nu_d^0$, which yields that $\nu_d^0 \approx \nu_{dj}$. The deuterium experimental rate of radial transfer of toroidal angular momentum calculated using this process is show in Figure 5.1.

The difference between the carbon and deuterium toroidal rotation velocities was calculated using Eq. (20) and added to the measured carbon toroidal rotation velocity to approximate the deuterium toroidal rotation velocity. This exercise, which only effected minute changes on the carbon toroidal rotation velocity profile, confirmed the validity of assuming a small difference between the carbon and deuterium toroidal rotation velocities. This confirmation supports the validity of the entire perturbation analysis and the accuracy of the ν_{dj} profile.

5.2

Deuterium Toroidal Rotation Velocity: $V_{\phi j}$

The perturbation analysis employed to derive an expression for ν_{dj} in the previous subsection centered on the lack of an appreciable difference between the toroidal rotation velocities of the carbon and deuterium ions. In confirming that this assumption is accurate[30], it is justifiable to represent the deuterium toroidal rotation velocity as approximately equal to the measurable carbon toroidal rotation velocity, which was shown in Fig. 4.5.

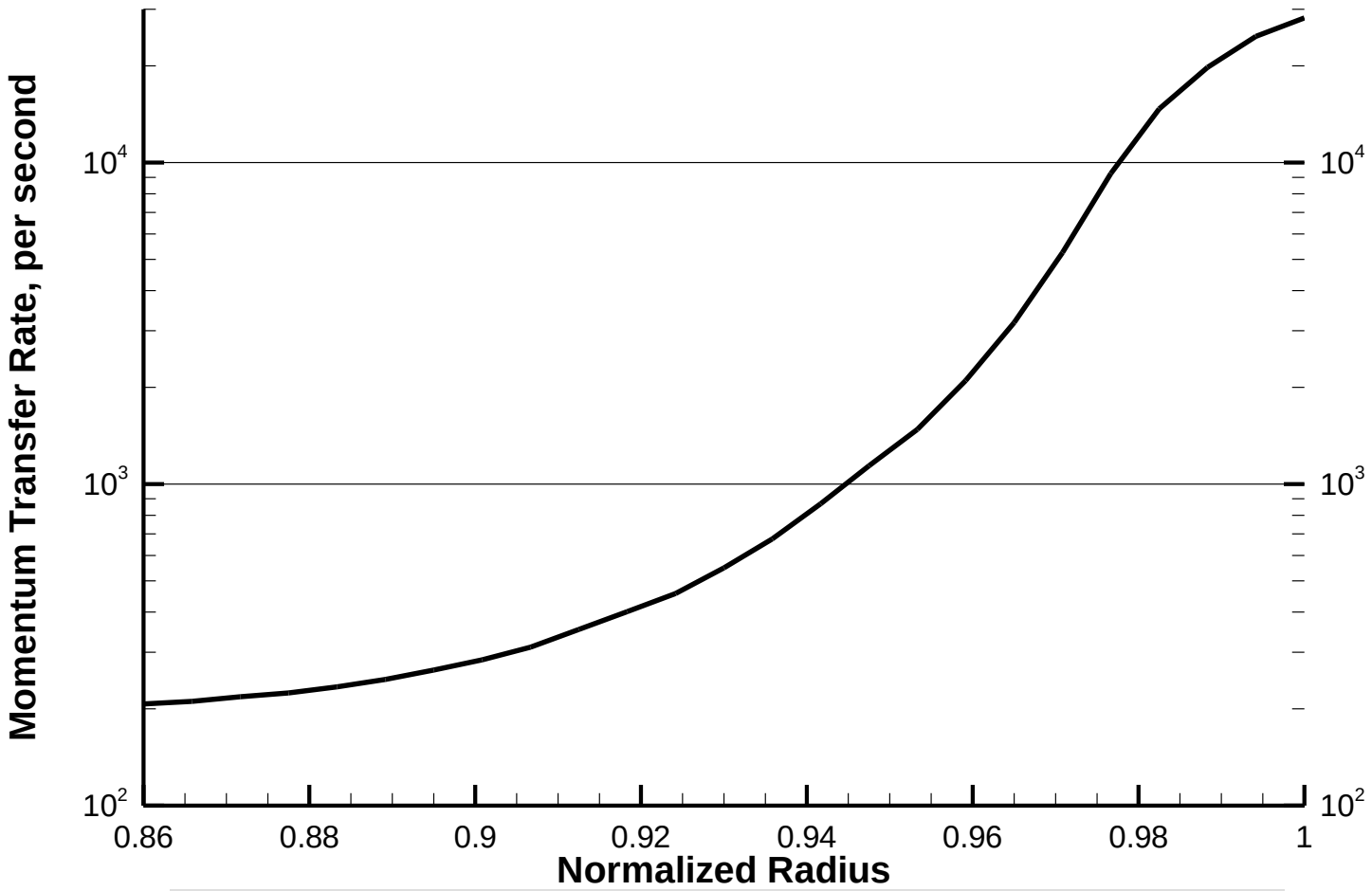

Figure 5.1 : Experimental Rate of Radial Transfer of Toroidal Angular Momentum.

5.3

Deuterium Poloidal Rotation Velocity: $V_{\theta j}$

The currently unmeasurable deuterium poloidal rotation velocity was calculated from poloidal momentum balance using Stacey-Sigmar poloidal rotation theory[30,35]. The equation for the deuterium poloidal velocity

$$\left(\frac{q\nu_{thj}f_j}{R}+\nu_{jk}+\nu_{atomj}\right)V_{\theta j}-\nu_{jk}V_{\theta k}=-\frac{e_jV_{rj}B_\phi}{m_j}+\frac{\nu_{thj}f_jq}{R}\left(\frac{B_\phi K^jT_jL_{Tj}^{-1}}{e_jB^2}+\frac{\nu_{thj}E_r}{B_\theta}\right) \qquad (22)$$

was evaluated using the measured experimental carbon poloidal rotation velocity, the major radius, the safety factor q, the atomic physics momentum transfer rate ν_{atomj}, and the thermal deuterium velocity ν_{thj}. The term $\eta_{0j}=n_jm_j\nu_{thj}qRf_j(\nu_{jj}^*)$ is Shaing's neoclassical viscosity coefficient[36], and K^j is a ratio of Hirshman-Sigmar coefficients defined in Ref. 35. The quantity $f_j=\frac{\varepsilon^{-3/2}\nu_{jj}^*}{[(1+\varepsilon^{-3/2}\nu_{jj}^*)(1+\nu_{jj}^*)]}$ is an interpolation formula connecting the collisional result $f_j=\frac{1}{\nu_{jj}^*}$ (where $\nu_{jj}^*=\frac{\nu_jqR}{V_{thj}}$) to the collisionless banana-plateau regime results.

This model does not take into account any viscously driven torques in the edge plasma due to scrape-off layer (SOL) flows, ion orbit loss, nor other poorly understood phenomena thought to affect rotation in the plasma edge. The possibility of such phenomena contribute uncertainty to this calculation.

In order to attempt to account for these factors, an expression for the carbon poloidal rotation velocity, which is measurable and shown in Fig. 4.5, was derived using

Stacey-Sigmar poloidal rotation theory. The same theory was then utilized to find an expression for the deuterium poloidal rotation velocity [Eq. (22)]. The difference between the measured and calculated carbon poloidal rotation velocity profiles was taken to be an approximation of the difference between the actual deuterium poloidal rotation velocity profile and the one calculated using Eq. (22). The difference between the carbon poloidal rotation velocity profiles was then added to the deuterium poloidal rotation velocity profile calculated using Eq. (22) to arrive at a "correct" profile for the deuterium poloidal rotation velocity. Figure 5.2 shows the profiles of the "correct" and calculated deuterium, and measured and calculated carbon poloidal rotation velocities.

5.4

The Pinch Velocity and Diffusion Coefficient

The deuterium pinch velocity was evaluated from Eq. (12) and the deuterium diffusion coefficient was evaluated from Eq. (11), using the "correct" deuterium poloidal rotation velocity calculated as discussed and the other inputs from Chapters 4 and 5. Both quantities are shown in Figure 5.3. The main contributions to the pinch velocity are from the deuterium poloidal rotation velocity and radial electric field terms, both of which have large magnitudes in the edge.

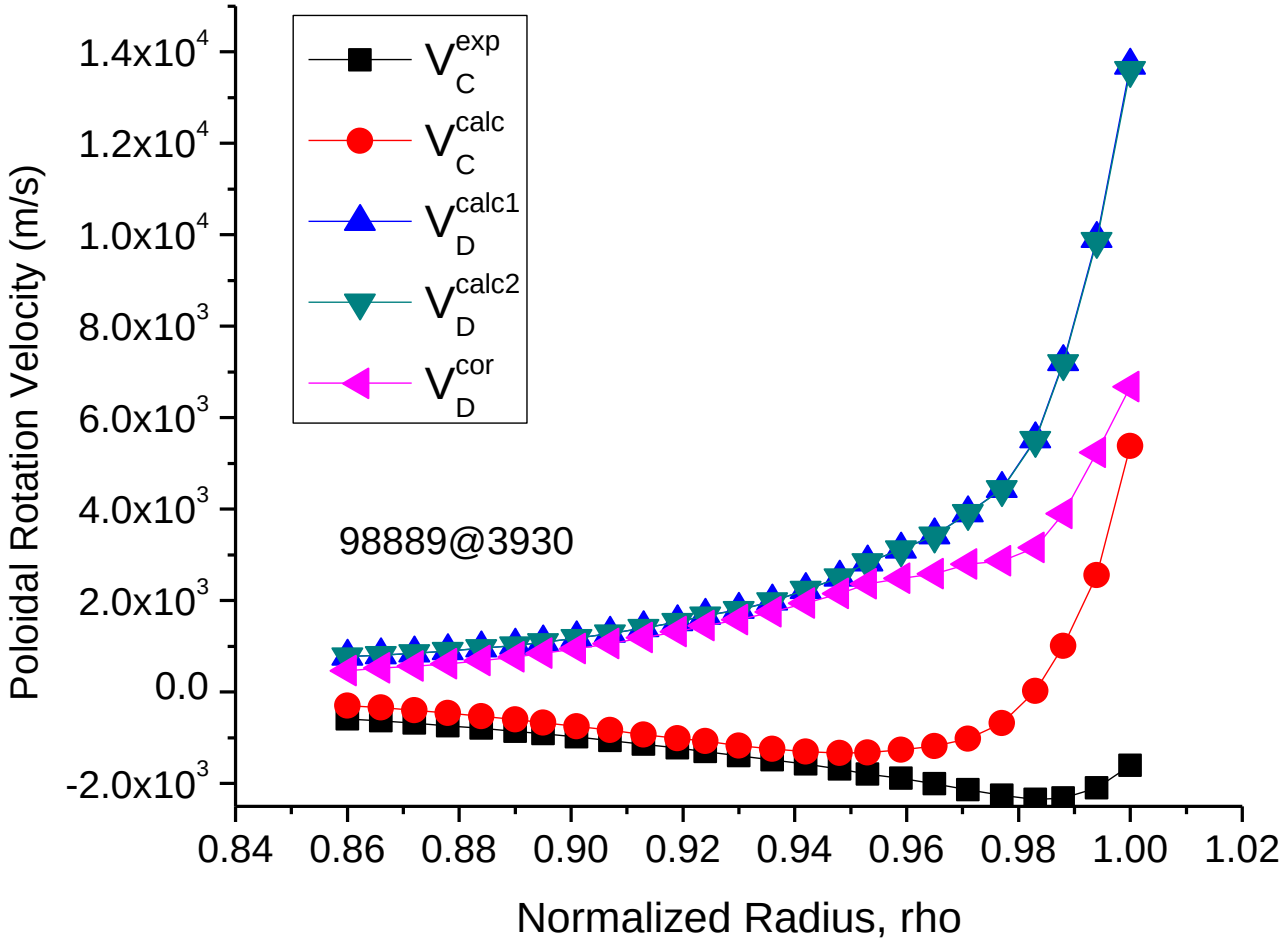

Figure 5.2 : Deuterium Poloidal Rotation Velocity. V_D^{calc2} can be disregarded.

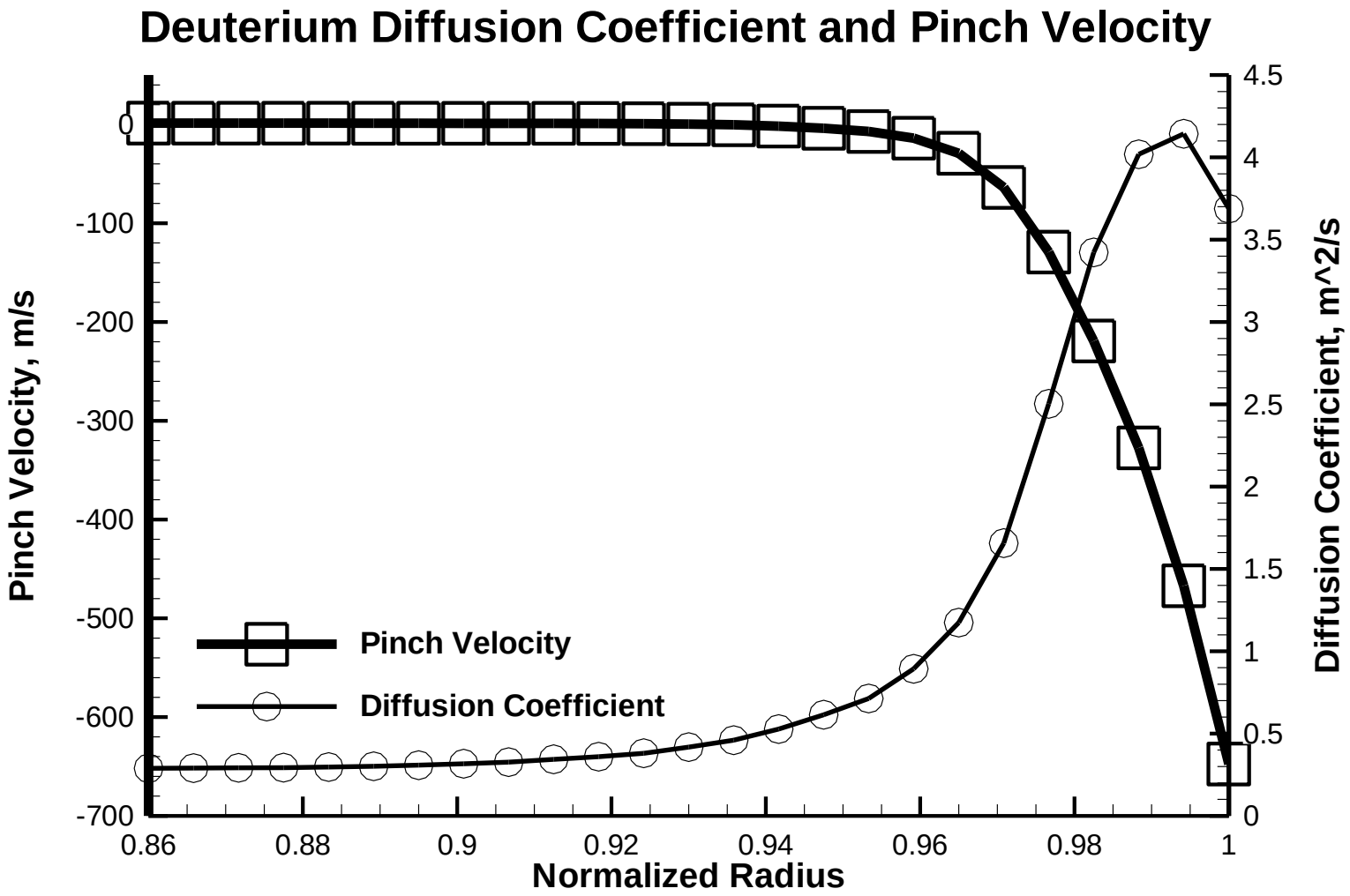

Figure 5.3 : Deuterium Diffusion Coefficient and Pinch Velocity.

Chapter 6

Numerical Methods

6.1

Numerical Algorithms for Solving the Generalized Diffusion Equation

Numerous sophisticated and well-tested methods of solving the neutron diffusion equation have been developed and adapted to calculate particle transport in plasmas. The major edge-transport codes, such as UEDGE and SOLPS, utilize such pure diffusion theory solution methods and are structured around them. Given this situation, it makes sense to investigate if the well-developed methods for solving the pure diffusion equation can be adapted to solve the generalized diffusion equation.

In this first investigation of the matter, the radial, one-dimensional generalized diffusion equation is considered in the slab geometry approximation. Standard finite-difference approximations are used in the discretization of Eq. (15); the widely used central-difference approximation is always used with the diffusive term and the central, backward, and forward difference approximations are used to evaluate the pinch term. After these approximations have been implemented, Gauss reduction[37], or forward elimination/backward substitution, is employed to solve the set of equations for the pressure at each point, and the known experimental temperatures are then used to calculate the density profiles through Eq. (6). These density profiles are then compared to the "exact" calculated density profiles to investigate the accuracy of the finite-difference algorithms used to numerically solve the generalized diffusion equation.

6.2

"Exact" Numerical Evaluation of Density Profile

The "exact" solution of Eq. (10) is useful as a benchmark solution for comparison with the solutions to the generalized diffusion equation. Dividing the second and third terms by the ion density in Eq. (10) results in

$$\frac{-1}{p_j}\frac{\partial p_j}{\partial r} = \frac{V_{rj} - V_{rj}^{pinch}}{D_j} \tag{23}$$

which is solved for the ion pressure by numerical integration between mesh points i and i+1

$$\begin{aligned} &\frac{1}{p}\frac{\partial p}{\partial r} = \frac{\partial(\ln p)}{\partial r} = \frac{V_{rj}^{pinch} - V_{rj}}{D} \\ &\int_i^{i+1} \frac{\partial(\ln p)}{\partial r} = \int_i^{i+1} \frac{V_{rj}^{pinch} - V_{rj}}{D} \\ &\ln p_{i+1} / p_i = \frac{\Delta}{2}\left(\frac{V_{rji+1}^{pinch} - V_{rji+1}}{D_{ji+1}} + \frac{V_{rji}^{pinch} - V_{rji}}{D_{ji}} \right) \end{aligned} \tag{24}$$

where Δ represents the interpoint interval width (mesh spacing), to obtain the "exact" pressure relation

$$p_{ji+1} = p_{ji} \exp\wedge\left[\frac{\Delta}{2}\left(\frac{\left(V_{rji+1}^{pinch} - V_{rji+1}\right)\Delta}{D_{ji+1}} + \frac{\left(V_{rji}^{pinch} - V_{rji}\right)\Delta}{D_{ji}} \right) \right] \tag{25}$$

The experimental deuterium ion temperature is then used to solve Eq. (6) for the density.

In order to evaluate Eq. (25), experimental and calculated data are used to determine V_{rj} from Eq. (13), V_{rj}^{pinch} from Eq. (12), and D_j from Eq. (11). This algorithm was used to advance the pressure inward from the value at the separatrix, which was

taken from experiment ($p_{j25} = p_{j25}^{\exp}$).

The main purpose of this paper is to investigate the differences between the "exact" numerical solutions of Eq. (25) and the finite-difference algorithm solutions to the generalized diffusion equation [Eq. (15)], using the same data to evaluate both equations. A secondary purpose is to compare these solutions with the independently measured experimental density profile.

6.3

Data Treatment and Mesh Spacing in the Numerical Solution

The measured and calculated plasma parameter profiles used for this study are flux surface averaged values plotted against the normalized radius at twenty-five points in the edge of the plasma ranging from $\rho = 1.0$ inwards, with a separation of $\bar{r} = .005$ m between points. In deriving the finite-difference approximations, the data values were assumed to be constant over the interval including the data point i as the midpoint.

6.4

Discretization of the Generalized Diffusion Equation

The discretization of Eq. (15), the generalized diffusion equation, is considered. This equation can be integrated over the interval $i - 0.5\Delta < r < i + 0.5\Delta$.

$$\int_{i-\frac{\Delta}{2}}^{i+\frac{\Delta}{2}} -\frac{\partial}{\partial r}\left(\frac{D_j}{T_j}\frac{\partial p_j}{\partial r}\right) + \int_{i-\frac{\Delta}{2}}^{i+\frac{\Delta}{2}} \frac{\partial}{\partial r}\left(\frac{p_j V_{rj}^{pinch}}{T_j}\right) = \int_{i-\frac{\Delta}{2}}^{i+\frac{\Delta}{2}} S_j \qquad (26)$$

The diffusion term is a perfect differential, and this integration leads to the well-known and widely used central difference approximation.

$$-\left(\frac{D_j}{T_j}\frac{\partial p_j}{\partial r}\right)_{i+\frac{\Delta}{2}}+\left(\frac{D_j}{T_j}\frac{\partial p_j}{\partial r}\right)_{i-\frac{\Delta}{2}}=-\left(\left(\frac{D_{ji+1}}{2T_{ji+1}}+\frac{D_{ji}}{2T_{ji}}\right)\frac{\left(p_{ji+1}-p_{ji}\right)}{\Delta}\right)+\left(\left(\frac{D_{ji}}{2T_{ji}}+\frac{D_{ji-1}}{2T_{ji-1}}\right)\frac{\left(p_{ji}-p_{ji-1}\right)}{\Delta}\right)$$

$$=\frac{1}{2\Delta}\left[\frac{-D_{ji+1}p_{ji+1}}{T_{ji+1}}+\frac{D_{ji+1}p_{ji}}{T_{ji+1}}-\frac{D_{ji}p_{ji+1}}{T_{ji}}+\frac{2D_{ji}p_{ji}}{T_{ji}}-\frac{D_{ji}p_{ji-1}}{T_{ji}}+\frac{D_{ji-1}p_{ji}}{T_{ji-1}}-\frac{D_{ji-1}p_{ji-1}}{T_{ji-1}}\right]$$

$$=\frac{1}{2\Delta}\left[\left(\frac{-D_{ji+1}}{T_{ji+1}}-\frac{D_{ji}}{T_{ji}}\right)p_{ji+1}+\left(\frac{D_{ji+1}}{T_{ji+1}}+\frac{2D_{ji}}{T_{ji}}+\frac{D_{ji-1}}{T_{ji-1}}\right)p_{ji}+\left(\frac{-D_{ji}}{T_{ji}}-\frac{D_{ji-1}}{T_{ji-1}}\right)p_{ji-1}\right]$$

(27)

The integral of the pinch term

$$\int_{i-\frac{\Delta}{2}}^{i+\frac{\Delta}{2}}\frac{\partial}{\partial r}\left(\frac{p_j V_{rj}^{pinch}}{T_j}\right)=\Delta\left[\frac{\partial}{\partial r}\left(\frac{p_j V_{rj}^{pinch}}{T_j}\right)\right]_i \tag{28}$$

was evaluated at point i in three different ways. In the forward difference approximation, the pinch term was evaluated by representing the derivative at point i with the forward difference approximation.

$$\Delta\left[\frac{\partial}{\partial r}\left(\frac{p_j V_{rj}^{pinch}}{T_j}\right)\right]_i=\left(\frac{p_{ji+1}V_{rji+1}^{pinch}}{T_{ji+1}}-\frac{p_{ji}V_{rji}^{pinch}}{T_{ji}}\right) \tag{29}$$

The backward difference approximation was implemented by representing the derivative of the pinch term at point i with the backward difference approximation.

$$\Delta\left[\frac{\partial}{\partial r}\left(\frac{p_j V_{rj}^{pinch}}{T_j}\right)\right]_i=\left(\frac{p_{ji}V_{rji}^{pinch}}{T_{ji}}-\frac{p_{ji-1}V_{rji-1}^{pinch}}{T_{ji-1}}\right) \tag{30}$$

In the central difference approximation, the derivative of the pinch term was evaluated with the central difference approximation.

$$\Delta\left[\frac{\partial}{\partial r}\left(\frac{p_j V_{rj}^{pinch}}{T_j}\right)\right]_i = \left(\frac{p_{ji+\frac{\Delta}{2}} V_{rji+\frac{\Delta}{2}}^{pinch}}{T_{ji+\frac{\Delta}{2}}} - \frac{p_{ji-\frac{\Delta}{2}} V_{rji-\frac{\Delta}{2}}^{pinch}}{T_{ji-\frac{\Delta}{2}}}\right) = \frac{1}{2}\left(\frac{p_{ji+1} V_{rji+1}^{pinch}}{T_{ji+1}} - \frac{p_{ji-1} V_{rji-1}^{pinch}}{T_{ji-1}}\right) \tag{31}$$

Since the ionization source rate is constant over the interval of integration in Eq. (26), the integral of the right hand side is simply $S_j\Delta$.

Combining the two terms on the left of Eq. (26) in each case, the finite-differenced representation of Eq. (15) takes the form of the set of equations

$$\left(a_{ii-1}^*\right) p_{i-1} + \left(a_{ii}^*\right) p_i + \left(a_{ii+1}^*\right) p_{i+1} = S_i^* \tag{32}$$

where the definitions of the a_{nm} coefficients and the source term are given by

$$a_{ii-1}^* = \frac{-D_{ji}}{2\Delta T_{ji}} + \frac{-D_{ji-1}}{2\Delta T_{ji-1}} + \alpha;\ a_{ii}^* = \frac{D_{ji+1}}{2\Delta T_{ji+1}} + \frac{D_{ji}}{\Delta T_{ji}} + \frac{D_{ji-1}}{2\Delta T_{ji-1}} + \beta;\ a_{ii+1}^* = \frac{-D_{ji+1}}{2\Delta T_{ji+1}} + \frac{-D_{ji}}{2\Delta T_{ji}} + \gamma;\ S_j^* = S_{ji}\Delta \tag{33}$$

The α, β, and γ terms in Eq. (33) depend on the type of finite difference approximation used for the pinch term and are displayed in Table 6.1.

Table 6.1 : Definitions of the Varying Terms Used in Eq. (33) Grouped by Finite-Difference Algorithm.

	Forward	Backward	Central
α	0	$\frac{-V_{rji-1}^{pinch}}{T_{ji-1}}$	$\frac{-V_{rji-1}^{pinch}}{2T_{ji-1}}$
β	$\frac{-V_{rji}^{pinch}}{T_{ji}}$	$\frac{V_{rji}^{pinch}}{T_{ji}}$	0
γ	$\frac{V_{rji+1}^{pinch}}{2T_{ji+1}}$	0	$\frac{V_{rji+1}^{pinch}}{2T_{ji+1}}$

Gauss Reduction[37] ("forward elimination backward substitution"), can be used to solve the set of Eqs. (32) exactly. Using this method[38], $\frac{a_{ii-1}}{a_{i-1i-1}}$ is multiplied by the (i-1)-th

equation, and this term is then subtracted from the i-th equation to eliminate the a_{ii-1} element in the i-th equation. The i-th equation (now missing the a_{ii-1} term) is then divided by a_{ii}. This process is repeated successively for i=1 through i=I-1. Then the set of equations is solved backwards by substitution using the formulae

$$\begin{aligned} \phi_{I-1} &= \alpha_{I-1} \\ \phi_{I-2} &= -A_{I-2}\phi_{I-1} + \alpha_{I-2} \\ &\vdots \\ \phi_i &= -A_i\phi_{i+1} + \alpha_{i+1} \end{aligned} \tag{34}$$

where the values for the parameters

$$\begin{aligned} A_1 &= \frac{a_{12}}{a_{11}}; \quad A_i = \frac{a_{ii+1}}{a_{ii} - a_{ii-1}A_{i-1}} \\ \alpha_1 &= \frac{S_1}{a_{11}}; \quad \alpha_i = \frac{S_i - a_{ii-1}\alpha_{i-1}}{a_{ii} - a_{ii-1}A_{i-1}} \end{aligned} \tag{35}$$

are calculated during the forward sweep. A known density boundary condition at the separatrix ($p_{25} = p_{25}^{\exp}$) and a zero current inner boundary condition ($p_1 = p_2$) are used. As shown in Figure 1.3, the electron density and ion temperature profiles are relatively constant towards the plasma core, allowing this inner boundary condition to be used confidently.

6.5

"Characteristic Diffusion Length" and Error Determination

Solving the source-free pinch-diffusion relation

$$\frac{1}{p_j}\frac{\partial p_j}{\partial r} = \frac{V_{rj}^{pinch}}{D_j} \tag{36}$$

by using the forward difference approximation for the derivative results in the solution

$$p_{ji+1} = p_{ji} e^{\Delta V_{rj}^{pinch}/D_j} \tag{37}$$

The "characteristic diffusion length" is

$$L \equiv \left| D_j / V_{rj}^{pinch} \right| \tag{38}$$

and generally, $\Delta \ll L$ is desired for accuracy.

Due to the sharply increasing pinch velocity magnitude in the edge, the "characteristic diffusion length" drops sharply near the separatrix, as shown in Figure 6.1.

It is instructive to investigate the intrinsic accuracy of the different finite-difference algorithms used to solve the generalized diffusion equation by comparing them with the exact solution of Eq. (15).

To obtain an approximate expression for the error inherent in using the forward finite-difference algorithm to solve the generalized diffusion equation (the error sought here is the error in calculating the value of the pressure at each point from the adjacent points using the forward finite-difference approximation algorithm), a source-free version of Eq. (15)

$$\frac{\partial^2 p_j}{\partial r^2} - \frac{V_{rj}^{pinch}}{D_j}\frac{\partial p_j}{\partial r} = 0 \tag{39}$$

is discretized using the forward difference approximation on the pinch term, and (always) the central difference approximation on the diffusion term.

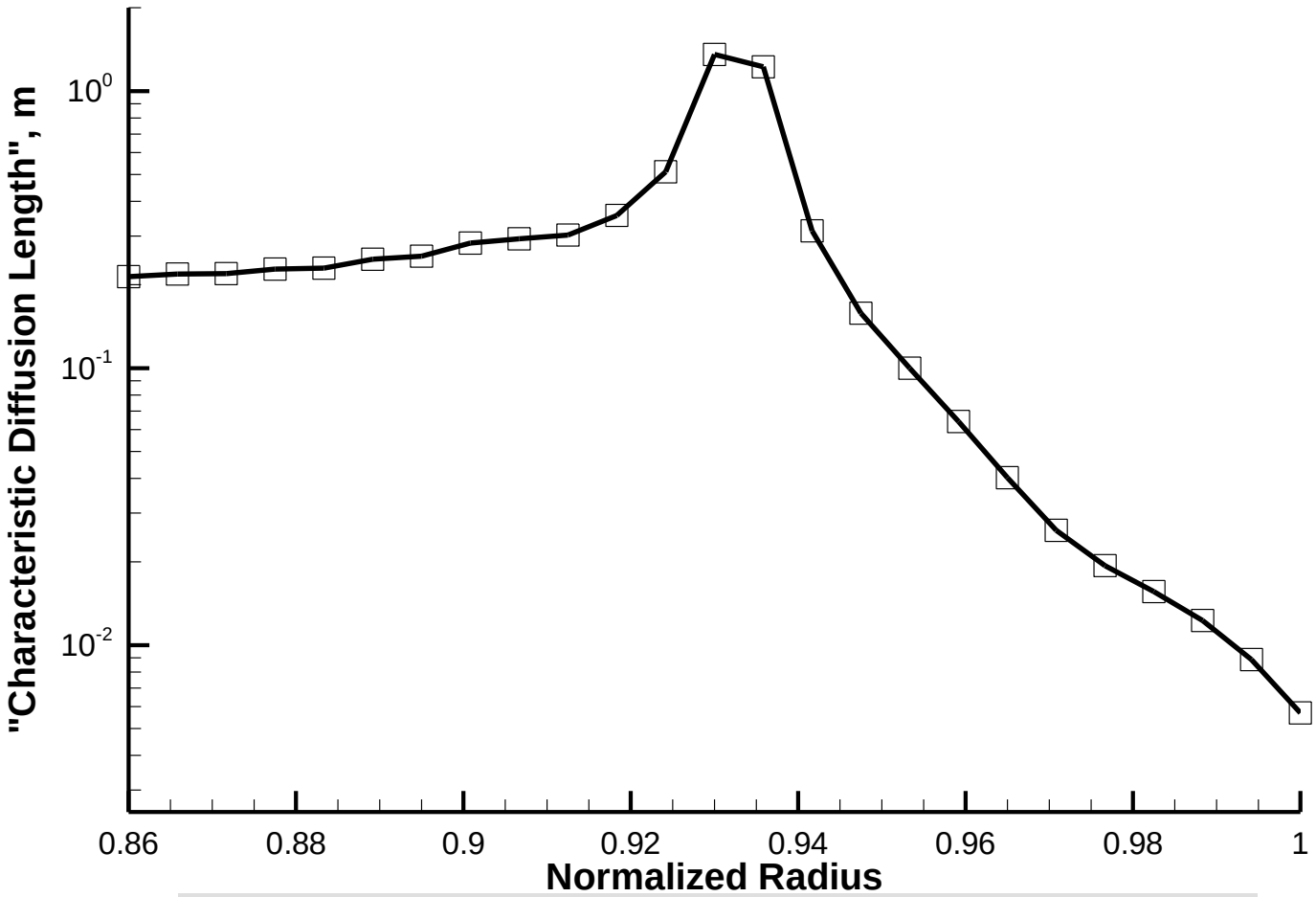

Figure 6.1 : Deuterium “Characteristic Diffusion Length”.

$$p_{ji+1} - 2p_{ji} + p_{ji-1} = \frac{\Delta V_{rj}^{pinch} p_{ji+1}}{D_j} - \frac{\Delta V_{rj}^{pinch} p_{ji}}{D_j} \tag{40}$$

A further approximation is made in deriving these expressions for the error in that the diffusion coefficient and pinch velocity are taken out of the derivatives, and assumed constant over the interval.

Equation (37) is used to generate an expression to replace the pressure ratios when Eq. (40) is rearranged, and

$$\frac{p_{ji+1} + p_{ji-1}}{p_{ji}} = 2 + \frac{\Delta V_{rj}^{pinch}}{D_j}\left(\frac{p_{ji+1}}{p_{ji}} - 1\right) \tag{41}$$

becomes

$$\left(\frac{p_{ji+1} + p_{ji-1}}{p_{ji}}\right)_{for\ diff} = 2 + \frac{\Delta V_{rj}^{pinch}}{D_j}\left(e^{\frac{\Delta V_{rj}^{pinch}}{D_j}} - 1\right) = 2 + \frac{\Delta}{L}\left(e^{\frac{\Delta}{L}} - 1\right) \tag{42}$$

while from Eq. (37)

$$\left(\frac{p_{ji+1} + p_{ji-1}}{p_{ji}}\right)_{exact} = e^{\frac{\Delta}{L}} + e^{-\frac{\Delta}{L}} \tag{43}$$

The subscript "for diff" represents the forward finite-difference algorithm for solving the source-free generalized diffusion equation, and the "exact" subscript refers to Eq. (37). The difference between the two expressions obtained from the two equations for the same value is taken to be the error inherent in using the forward finite-difference algorithm to numerically solve the source-free generalized diffusion equation.

$$\begin{aligned}\left(\frac{p_{ji+1} + p_{ji-1}}{p_{ji}}\right)_{for\ diff} - \left(\frac{p_{ji+1} + p_{ji-1}}{p_{ji}}\right)_{exact} &= error \\ &= 2 + \frac{\Delta}{L}\left(e^{\frac{\Delta}{L}} - 1\right) - e^{\frac{\Delta}{L}} - e^{-\frac{\Delta}{L}}\end{aligned} \tag{44}$$

The exponentials are expanded to obtain

$$error = 2 + \frac{\Delta}{L}\left(\left(1+\frac{\Delta}{L}+\frac{\Delta^2}{2L^2}+\frac{\Delta^3}{6L^3}\right)-1\right)-\left(1+\frac{\Delta}{L}+\frac{\Delta^2}{2L^2}+\frac{\Delta^3}{6L^3}\right)-\left(1-\frac{\Delta}{L}+\frac{\Delta^2}{2L^2}-\frac{\Delta^3}{6L^3}\right)$$

(45)

After simplification, the error is found to be proportional to the mesh spacing over the "characteristic diffusion length", all cubed. A similar method is used to determine the expressions for the error resulting from the use of the backward and central finite-difference algorithm. The expressions for the error are

$$error \cong \frac{1}{2}\left(\frac{\Delta}{L}\right)^3 \begin{cases} 1-\frac{1}{3}\frac{\Delta}{L}+\ldots & \textit{backward difference} \\ 1 & \textit{central difference} \\ 1+\frac{1}{3}\frac{\Delta}{L}+\ldots & \textit{forward difference} \end{cases} \quad (46)$$

when the forward, backward, and central finite-difference algorithms are used to solve the source-free generalized diffusion equation. These expressions are meant to approximate the error resulting from solving the normal generalized diffusion equation [Eq. (15)] using the finite-difference algorithms.

The error is very sensitive to the mesh spacing size and to the local value of the "characteristic diffusion length", L, as can be seen by comparing Figs. 6.1 and 6.2a. Figure 6.2a displays the error of using the backwards finite-difference algorithm to solve the source-free generalized diffusion equation as a function of mesh spacing. Clearly, a small value of Δ/L is required for precision when solving the generalized diffusion equation using finite-difference approximations. The error is not sensitive to the specific finite-difference algorithm except when Δ/L approaches unity, which happens for the larger mesh spacings just inside the separatrix. This sensitivity is shown in detail in

Figure 6.2b. From Eq. (46), the backward difference algorithm should be the most accurate, then the central difference algorithm. The errors predicted by Eqs. (46) are plotted in Fig. 6.2b for different choices of the finite-difference algorithm and mesh spacing; the error of the backward difference is the lowest, then the central difference, then the forward difference. At smaller mesh spacings below 0.25 cm, the solution sensitivity to the three finite-difference algorithms is small, and the error at these mesh spacings is not shown in Figure 6.2b. The backwards finite-difference algorithm error shown in Figure 6.2a can be taken as roughly representative of the error of the central and forward finite-difference algorithms for these smaller mesh spacings. The implication is that for a fixed mesh spacing, the error becomes larger in the edge where the pinch velocity becomes large. This suggests the use of a variable mesh algorithm with finer spacing in the edge in order to maintain an acceptable upper bound on the error at all locations while minimizing computing costs.

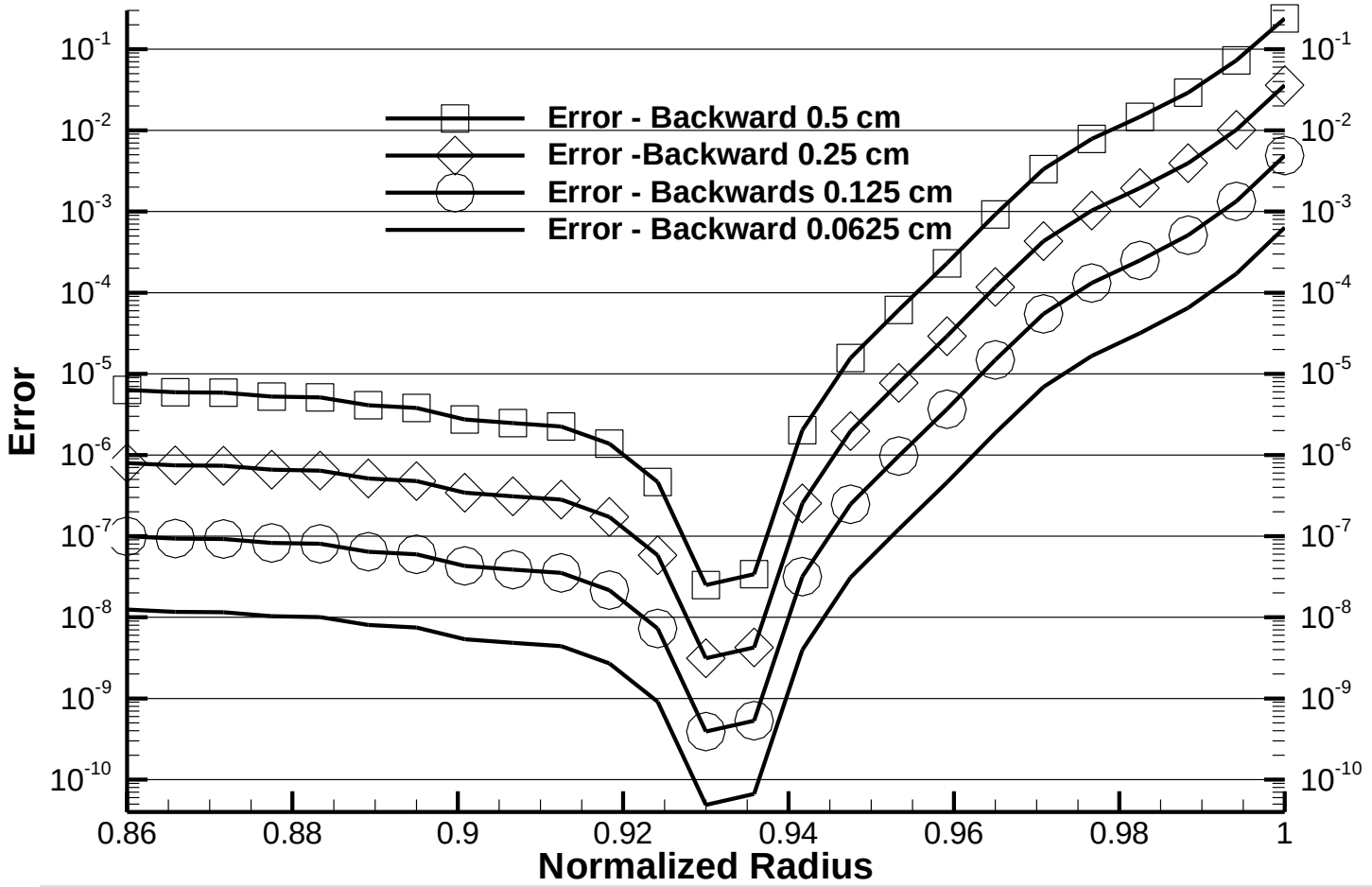

Figure 6.2a : Error of the Backwards Finite-Difference Discretization Algorithm for Various Mesh Spacings.

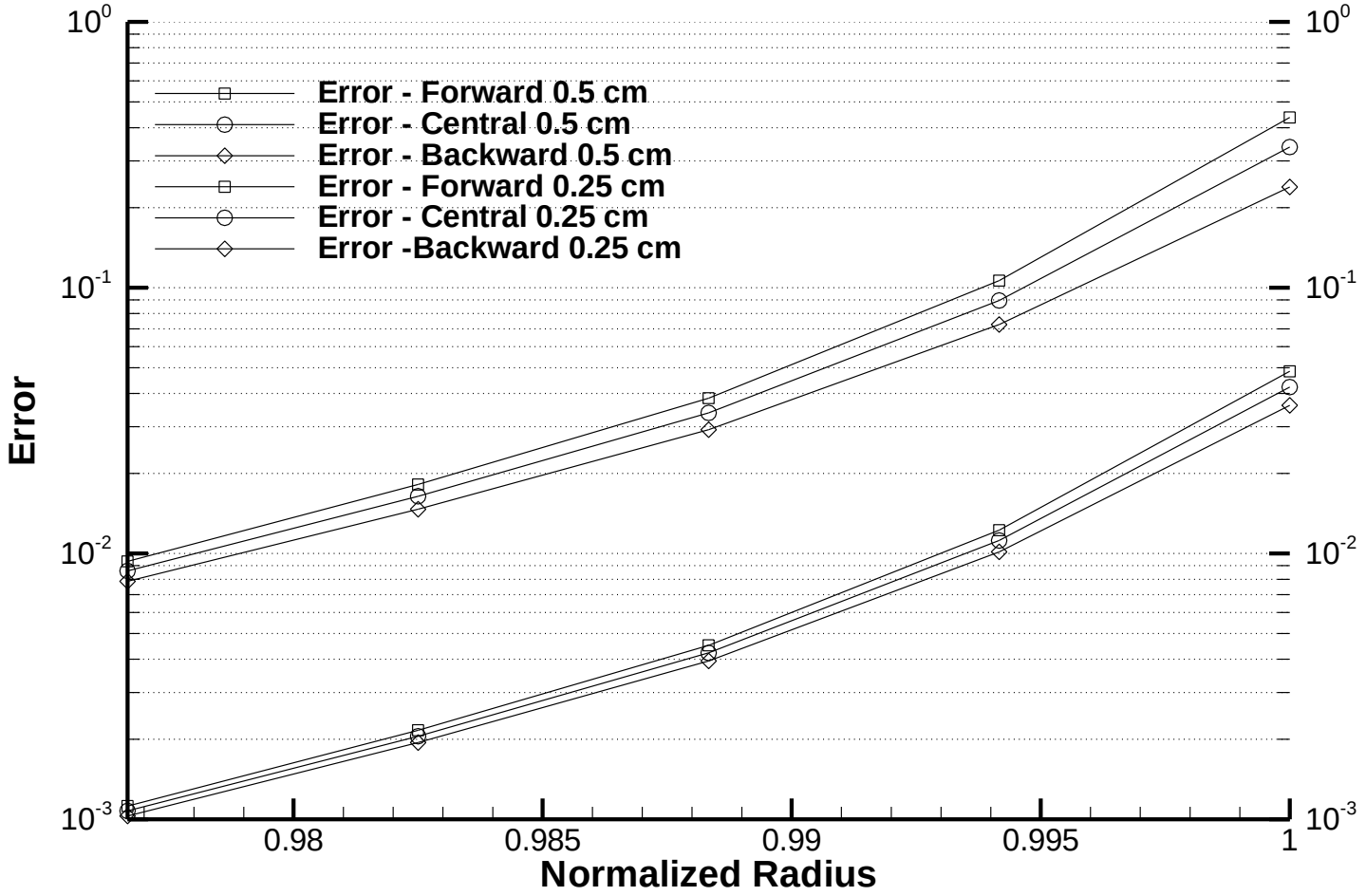

Figure 6.2b : Error of Various Finite-Difference Discretization Algorithms Near the Separatrix.

Chapter 7

Numerical Results

The generalized diffusion equation was solved using the three finite-difference approximation algorithms for four different mesh sizes, which were the original mesh of 0.5 cm, and the finer meshes of 0.25 cm, 0.125 cm, and 0.0625 cm. The pinch-diffusion relation was also solved for the "exact" profile at these same mesh sizes. The data for the three finer meshes was obtained by interpolating the 0.5 cm data to a finer scale

Figures 7.1 compare the solutions obtained by numerically solving the generalized diffusion equation [Eq. (15)] using the finite-difference approximation algorithms with both the "exact" numerical integration solution of Eq. (23) and the measured ion density for different choices of mesh spacing. It is clear that reducing the mesh spacing improves the agreement between the generalized diffusion equation solutions and the "exact" solution of Eq. (23), as would be expected from fact that the error $\approx (\Delta/L)^3$ of the finite-difference algorithms is strongly dependent on the mesh spacing. The differences among the solutions corresponding to the three finite-difference algorithms also decrease with finer mesh spacing, as predicted by Eqs. (46). The differences between the solutions of the generalized diffusion equation and the "exact" solution are consistent with the error analysis displayed in Fig. 6.2b.

It should be noted that the generalized diffusion equation is always solved with a known separatrix boundary condition at $\rho = 1.0$ on the right and that there is a large error (up to ~60% with a 0.5 cm mesh spacing and the forward-difference algorithm) in the generalized diffusion equation solution just inside the separatrix, as shown in Figs. 6.2a

and 7.1. This error causes an over-prediction of the solution just inside the separatrix. This over-prediction is then propagated inward (quite accurately, due to the increased accuracy of the solution algorithm at the points towards the core) by the solution algorithm, which calculates the pressure values at i based on the values of the pressure at the adjacent mesh points. This links the over-predicted edge pressure values in the edge to the inner values, causing them to be over-predicted as well. This results in a discrepancy between the finite-difference algorithm solutions to the generalized diffusion equation and the "exact" solution that is present across the entire range, despite most contributions to the error being limited to the outer third of the range. The effect of the larger error magnitude just inside the separatrix on the solution over the entire pedestal is illustrated in Figs. 7.1 and 7.2.

Although it is not the purpose of this paper to analyze the differences between prediction and experiment, the experimental ion densities (electron densities measured by Thomson scattering and corrected for the measured carbon impurity density) have been included in Figs. 7.1 and 7.2.

The differences between the "exact" solution and the experimental density are attributable to imprecision in the measurement and calculation of the parameters used to solve Eq. (23) and weaknesses in the slab model used in this study.

The only parameter that is very likely to be imprecise is the deuterium poloidal rotation velocity, due to the lack of reliable theoretical models and the current impossibility of measuring it. This inaccuracy is thought to be a major contributor to the discrepancy between the measured and "exact" solution profiles. Results from simple experimentation have shown that the solutions to the generalized diffusion equation are

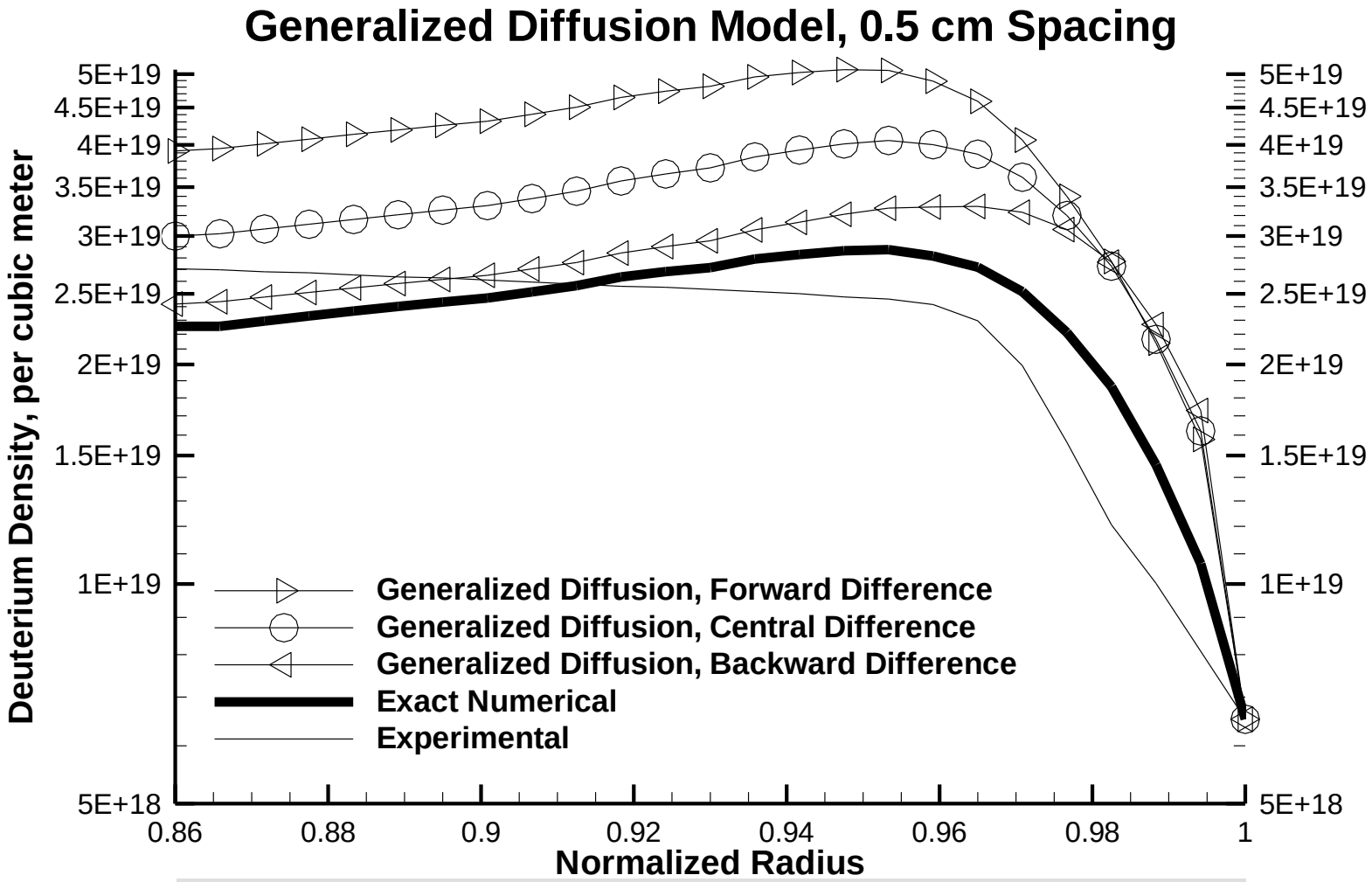

Figure 7.1a: Comparison of Calculated and Measured Deuterium Densities, 0.5 cm Mesh Spacing

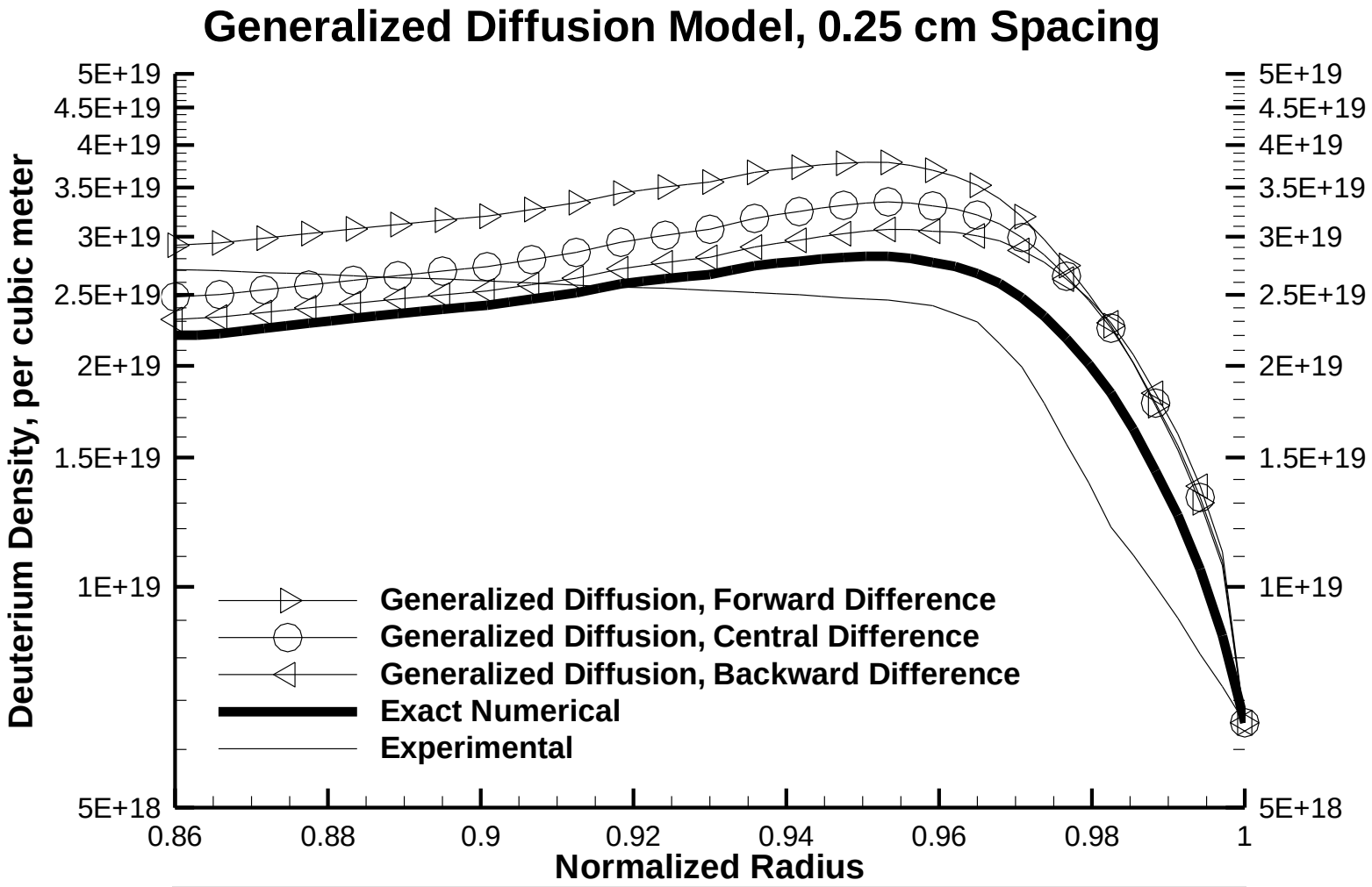

Figure 7.1b : Comparison of Calculated and Measured Deuterium Densities, 0.25 cm Mesh Spacing

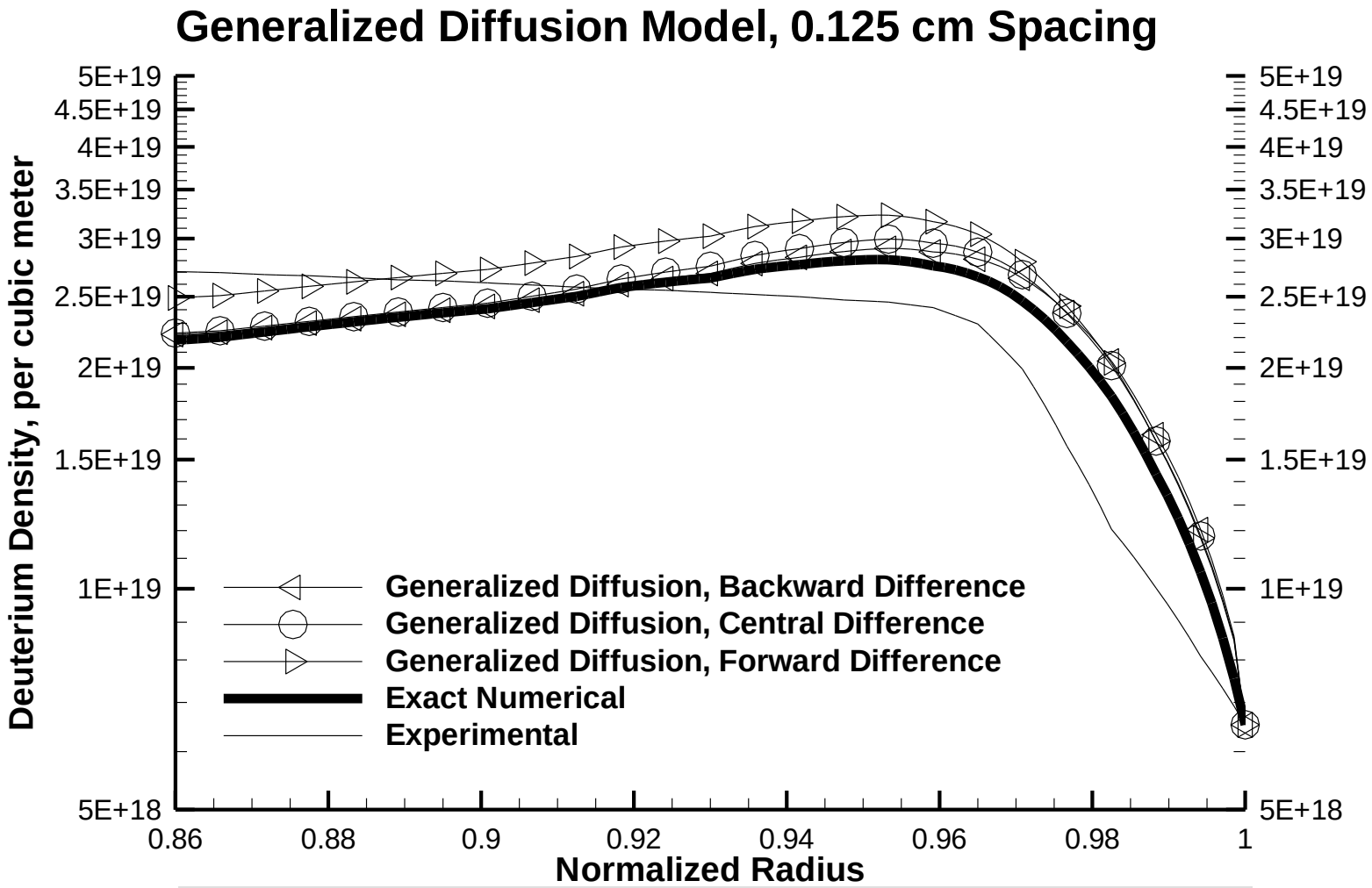

Figure 7.1c : Comparison of Calculated and Measured Deuterium Densities, 0.125 cm Mesh Spacing

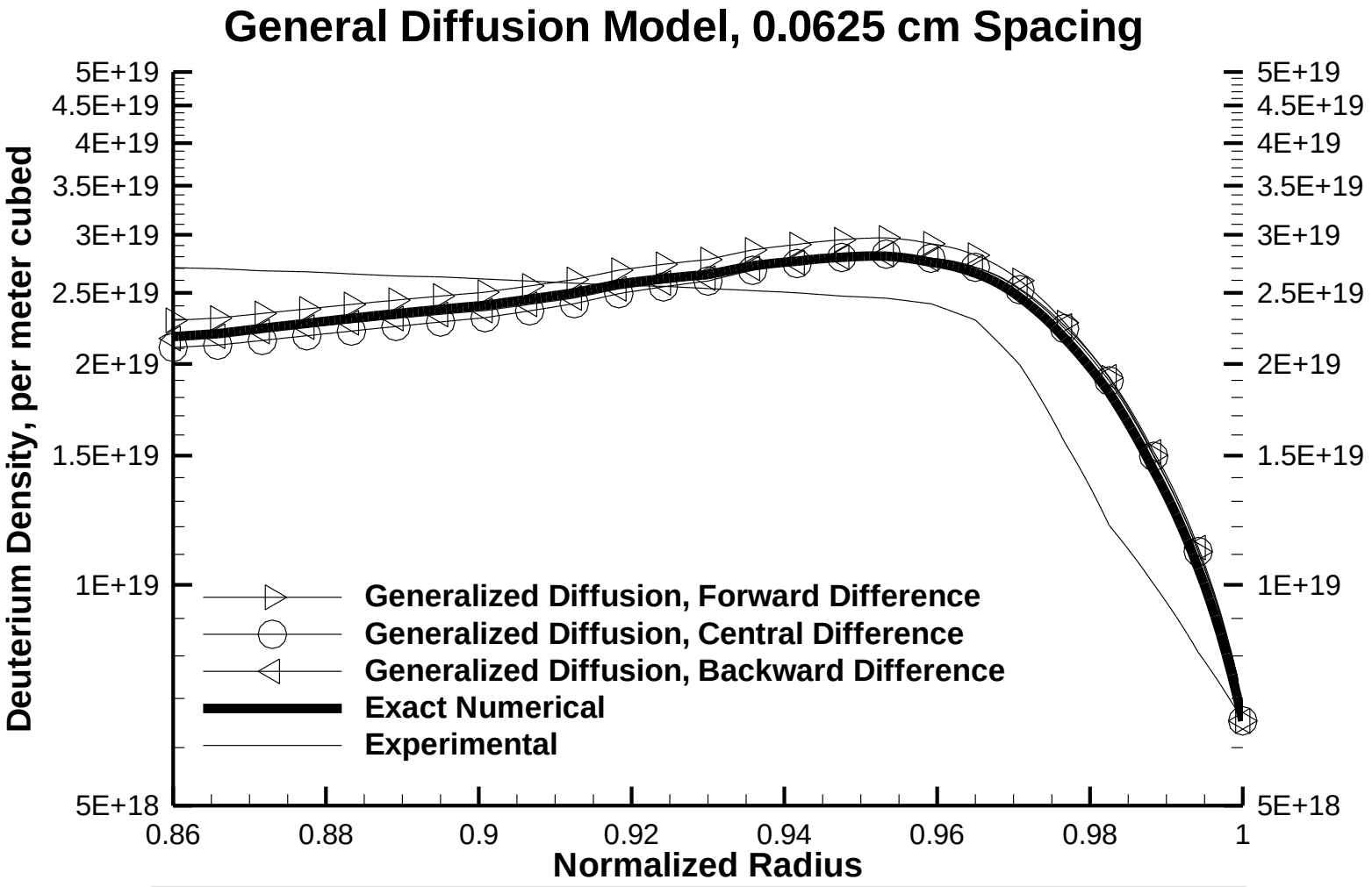

Figure 7.1d : Comparison of Calculated and Measured Deuterium Densities, 0.0625 cm Mesh Spacing

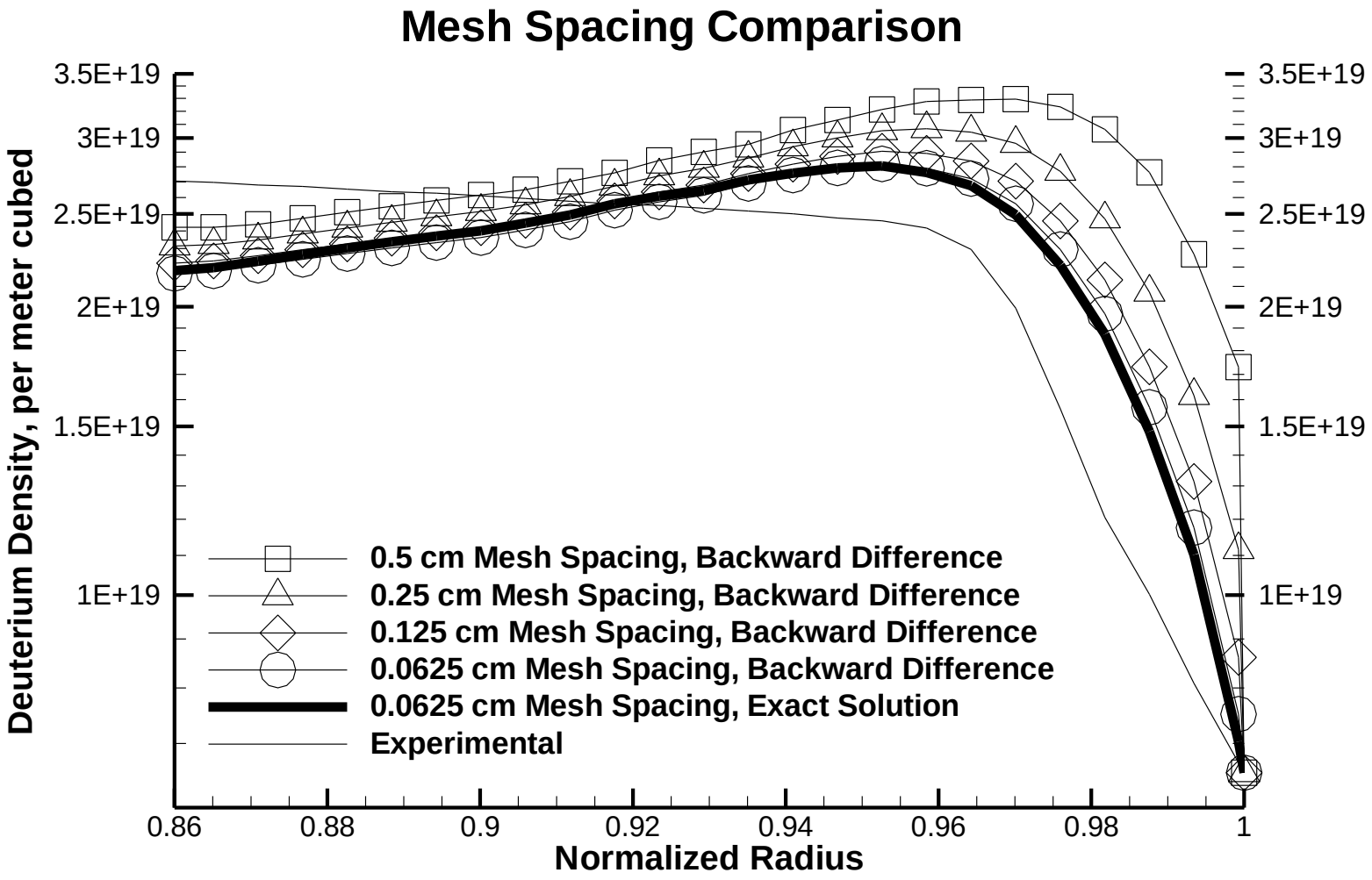

Figure 7.2 : Sensitivity of Backwards Finite-Difference Algorithm Solution to Mesh Spacing.

very sensitive to any manipulation of the "correct" deuterium poloidal rotation velocity, further supporting this hypothesis. The assumptions made in deriving Eq. (23) that take the carbon and deuterium logarithmic pressure gradients to be the same are not thought to contribute significantly to the error.

Another major contributor to the difference between the "exact" and measured profiles, especially in the inner part of the range, is the limitations of the slab model used in this work. The measured data uses a cylindrical model, and the distinct discrepancy between the "exact" solution and measured density profiles can be explained by a lack of radially inward particle flows at poloidal locations above and below the outboard horizontal midplane that would be present in a cylindrical model, but are not taken into account in the slab model.

Chapter 8

Summary and Conclusions

The large pinch velocity in the plasma edge of H-mode tokamak discharges requires that a pinch-diffusion relation for the particle flux be used in order to satisfy momentum balance; this leads to a generalized diffusion theory that includes a pinch term. A numerical investigation has been completed into the possibility of representing and solving this generalized diffusion equation by using the same type of finite-difference approximations and solution algorithms that are utilized with pure diffusion theory and employed in major plasma edge codes. The error of the finite-difference algorithm solutions of the generalized diffusion equation was shown to be approximately proportional to $(\Delta/L)^3$, where Δ is the mesh spacing and $L = \left| D_j / V_{rj}^{pinch} \right|$ is the "characteristic diffusion length". This error was shown to be quite large just inside the separatrix, where *L* becomes small due to a large pinch velocity. This may cause an error in the density solution that propagates into the pedestal region unless the mesh spacing is quite small just inside the separatrix. The implication is that a variable mesh spacing should be used for solving the generalized diffusion equation in the plasma edge, with the mesh being finely spaced just inside the separatrix where the pinch velocity is large. By making use of such a variable mesh spacing, it should be possible to extend existing diffusion theory codes to solve the generalized diffusion equation and correctly represent particle transport in the edge pedestal in a way that satisfies momentum balance.

Several research avenues for further exploration of the conclusions reached by this work can be readily identified. Since it has been shown that it is possible to

accurately solve the generalized diffusion equation using the finite-difference methodology that is associated with the pure diffusion model, the next logical step would be a study of implementing the generalized diffusion equation into the major edge transport codes. To improve the accuracy of the calculations, a variable mesh could be used, and more sophisticated assumptions about the parameter profiles between data points, such as a finite-element analysis, could be employed. Additionally, using a cylindrical model instead of a slab model would likely improve agreement with experiment in the inner part of the analyzed range.

Advancements in the theoretical understanding of the deuterium poloidal rotation velocity or the development of tools to measure it would be invaluable in conducting a definitive analysis of the pinch-diffusion model and the generalized diffusion equation.

REFERENCES

[1] *Our Star the Sun*. 1/20/11. Retrieved March 17, 2011 From http://sohowww.nascom.nasa.gov/classroom/sun101.html

[2] Edson, Jason and Hannah Cohen. 11/9/1998. *Two Important Fusion Reactions*. Retrieved March 17, 2011 From http://fusedweb.llnl.gov/CPEP/Chart_Pages/2.TwoFusionReactions.html

[3] *tokamak*. In *Merriam-Webster Online Dictionary*. Retrieved March 17, 2011, From http://www.merriam-webster.com/dictionary/tokamak

[4] *Building ITER*. Retrieved March 17, 2011 From http://www.iter.org/proj/buildingiter

[5] Jarvis, O. N. *4.7.4 Nuclear Fusion*. in *Kaye and Laby Tables of Physical and Chemical Constants*. Retrieved March 17, 2011 From http://www.kayelaby.npl.co.uk/atomic_and_nuclear_physics/4_7/4_7_4b.html

[6] Maggi, C. F. 2010 *Nucl. Fusion* **50** 066001.

[7] Osborne, T. H., R. J. Groebner, L. L. Lao, A. W. Leonard, R. Maingi, R. L. Miller, G. D. Porter, D. M. Thomas and R. E. Waltz 1997 *Proc. of the 24th European Conf. on Controlled Fusion and Plasma Phys.*, Berchtesgaden, Germany, 1997 (European Physical Society: Pettit-Lancy, Switzerland) Volume 21A, Part III, p.

1101.

[8] Greenwald, M., R. L. Boivin, F. Bombarda, P. T. Bonoli, C. L. Fiore, D. Garnier, J. A. Goetz, S. N. Golovato, M. A. Graf, R. S. Granetz, S. Horne, A. Hubbard, I. H. Hutchinson, J. H. Irby, B. LaBombard, B. Lipschultz, E. S. Marmar, M. J. May, G. M. McCracken, P. O'Shea, J. E. Rice, J. Schachter, J. A. Snipes, P. C. Stek, Y. Takase, J. L. Terry, Y. Wang, R. Watterson, B. Welch and S. M. Wolfe 1997 *Nucl. Fusion* **37** 793.

[9] Suttrop, W., M. Kaufmann, H. J. de Blank, B. Brusehaber, K. Lackner, V. Mertens, H. Murmann, J. Neuhauser, F. Ryter, H. Salzmann, J. Schweinzer, J. Stober, H. Zohm, and the ASDEX Upgrade Team 1997 *Plasma Phys. Control. Fusion* **39** 2051.

[10] Kotschenreuther, M., W. Dorland, Q. P. Liu, G. W. Hammett, M. A. Beer, S. A. Smith, A. Bondeson and S. C. Cowley 1996 *Proc. of the 16th Int. Conf. on Fusion Energy*, Montreal, Canada, 1996, (IAEA Vienna) Volume 2, p. 371.

[11] Kinsey, J.E., G. Bateman, T. Onjun, A. H. Kritz, A. Pankin, G. M. Staebler and R. E. Waltz 2003 *Nucl. Fusion* **43** 1845.

[12] St. John, H. E., T. S. Taylor, Y. R. Lin-Liu, and A. D. Turnbull 1995 *Proceedings of the 15th International Conference on Plasma Physics and Controlled Nuclear Fusion Research*, Seville, Spain, 1994, (IAEA Vienna) Volume 3, p. 603.

[13] Stacey, W. M. 1998 *Phys. Plasmas* **5** 1015; 2001 **8** 3673; 2000 Nucl. Fusion **40** 965.

[14] Pereverzev, G. V., and P. N. Yushmanov, "ASTRA: Automated System for Transport Analysis". February 2002, Technical Report, IPP 5/98, Max-Planck Institut fur Plasmaphysik.

[15] Scheider, R., X. Bonnin, K. Borrass, D. P. Coster, H. Kastelewicz, D. Reiter, V. A. Rozhansky, and B. J. Braams 2006 Contrib. Plasma Phys. **46** 3.

[16] Rognlien T. D., M. E. Rensink, and G. R. Smith 2007 "User Manual for the UEDG Edge- Plasma Transport Code" *Lawrence Livermore National Laboratory Report UCRL-ID-137121*, 10 Jan. 2000 (Updated 23 Feb 2007).

[17] Rognlien, T. D., and M. E. Rensink 2002 *Fusion Engineering and Design* **60** 497.

[18] Callen, J. D., R. J. Groebner, T. H. Osborne, J. M. Canik, L. W. Owen, A. Y. Pankin, T. Rafiq, T. D. Rognlien, and W. M. Stacey 2010 *Nucl. Fusion* **50** 064004.

[19] Stacey, W. M. 2004 *Phys. Plasmas* **11** 5487.

[20] Stacey, W. M. 2008 *Contrib. Plasma Phys.* **48** 94.

[21]Artsimovich, L. A. 1966 Plasma Phys. Controlled Nucl. Fusion Res., **2**, 595, 1966.

[22]Gorbunov, E. P. Plasma Phys. Controlled Nucl. Fusion Res. 2, 629, 1966.

[23] Coppi, B., and N. Sharkey 1981 *Nucl. Fusion* **21** 1363.

[24]Rensink, M. E., S. L. Allen, A. H. Futch, D. N. Hill, G. D. Porter and M. A. Mahdavi 1993 *Phys. Fluids B* **5** 2165.

[25] Luxon, J. 2002 *Nucl. Fusion* **42** 614.
Phys. Fluids B **5** 2165.

[26] Stacey, W. M., and R. J. Groebner 2007 *Phys. Plasmas* **14** 012501.

[27] Groebner, R. J., T. H. Osborne, A. W. Leonard and M. E. Fenstermacher 2009 *Nucl. Fusion* **49** 045013.

[28] Groebner, R. J., A. W. Leonard, P. B. Snyder, T. H. Osborne, C. F. Maggi, M. E. Fenstermacher, C. C. Petty, and L. W. Owen 2009 *Nucl. Fusion* **49** 085037.

[29] Kallenbach, A., Y. Andrew, M. Beurskens, G. Corrigan, T. Eich , S. Jachmich, M. Kempenaars, A. Korotkov, A. Loarte, G. Matthews , P. Monier-Garbet, G. Saibene , J. Spence, W. Suttrop and JET EFDA Contributors 2004 *Plasma Phys. Control. Fusion* **46** 431.

[30] Stacey, W. M., and R. J. Groebner 2008 *Phys. Plasma* **15** 012503.

[31] Miller, R. L., M. S. Chu, J. M. Greene, Y. R. Lin-Liu, and R. E. Waltz 1998 *Phys. Plamas* **5** 973.

[32] Groebner, R. J. General Atomics, personal communication (2010).

[33] Gohil, P., K. H. Burrell, R. J. Groebner, J. Kim, W. C. Martin, E. L. McKee, and R. P. Seraydarian 1992 *Proc. of the 14th Symposium on Fusion Engineering*, San Diego, California, 1992 (IEEE New York) Volume 2, p. 1199.

[34] Baylor, L. R., K. H. Burrell, R. J. Groebner, W. A. Houlberg, D. P. Ernst, M. Murakami, and M. R. Wade. 2004 *Phys. Plasmas* **11** 3100.

[35] Stacey, W. M. 2008 *Phys. Plasmas* **15** 012501.

[36] Stacey, W. M., A. W. Bailey, D. J. Sigmar, and K. C. Shaing 1985 *Nucl. Fusion* **25** 463.

[37] Press, William H., Flannery, Brian P., Teukolsky, Saul A., Vetterling, William T. *Numerical Recipes – The Art of Scientific Computing (Fortran Version).* New York City: Cambridge University Press (1986).

[38] Stacey, W. M. *Nuclear Reactor Physics, Vol. 1*. Weinheim: Wiley-VCH (2001).